



An Experimental Study Into the Effect of Damage on the Capacitance of Structural Composite Capacitors

T. CARLSON^{1,*} and L. E. ASP^{1,2}

¹Swerea SICOMP AB, Box 104, 43122 Mölndal, Sweden

²Luleå University of Technology, 97187 Luleå, Sweden

KEYWORDS

multifunctional composites
layered structures
electrical properties
matrix cracking

ABSTRACT

This paper presents the work to characterise the effects of tensile induced matrix cracks on capacitance of structural composite capacitor materials. The study is based on earlier work within the field of multifunctional materials where mechanical and electrical properties have been characterised. Effects of damage on electrical properties have, however, not been covered by earlier studies.

The structural capacitor materials were made from carbon fibre/epoxy pre-pregs as structural electrodes with thermoplastic PET as the dielectric separator. NaOH etching was used as a route for improved adhesion between the epoxy and PET to ensure matrix cracking in the CFRP electrodes occurred prior to delamination between the electrodes and the PET separator.

A method to induce and measure the effect of the matrix cracks on electrical properties was successfully developed and used in this study. The method is based on a simple tensile test and proved to be quick and easy to perform with consistent results. The structural capacitor material was found to maintain its capacitance even after significant intralaminar matrix cracking in the CFRP electrodes from high tensile mechanical loads.

© 2014 DEStech Publications, Inc. All rights reserved.

1. INTRODUCTION

The need for lightweight design and electrification are ever growing in consumer products, ranging from phones and laptops to road vehicles, etc. To meet these needs, novel approaches in material and product development are required. An elegant way to achieve lightweight energy storage is realisation of multifunctional materials and/or components, performing several tasks at once. This approach is particularly attractive since there is a limitation to the weight reduction achievable by optimisation of individual single purpose components and devices.

Chung and Wang [1] proposed the idea to exploit the semi-conductive nature of carbon fibres in “structural electronics” and to use CFRP laminas to make structural ca-

pacitors. The idea was realised in a follow-on study by Luo and Chung [2] making thin structural capacitors from carbon fibre epoxy pre-preg laminate electrodes and different paper dielectric separators. Baechle [3], O’Brien [4], Wetzel [5] and co-workers have expanded the idea by making structural capacitors employing glass fibre/epoxy pre-preg as the dielectric separator with metalized polymer films as electrodes. More recently, Yurchak *et al.* [6] investigated the interlaminar shear strength of the metalized film electrode and the glass fibre composite separator for these devices. The study showed interlaminar shear strength as high as 39.6 MPa between the metalized polyimide electrode and the epoxy based glass fibre composite separator. The approach in [6] is very similar to earlier work performed by Carlson *et al.* [7–11]. Carlson *et al.* investigated multifunctional performance of a series of structural capacitors made in the spirit of Luo and Chung [2], employing carbon fibre composite electrodes and dielectric separator made from dif-

*Corresponding author. E-mail: tony.carlson@swerea.se, Tel: +46(0)31 706 6376, Fax: +46(0)31 276130

ferent surface weight printing paper or polymer films. The concept of making capacitors with carbon fibre epoxy pre-preg electrodes separated by a thin polymer film was found to be most promising [7–11].

The objective of the current investigation was to determine the influence of damage caused by tensile loading on the electrical performance of structural capacitor materials of the type developed in previous studies [10–11]. Intra-laminar matrix cracks are well known to affect mechanical performance of a composite material, as reported by Varna *et al.* [12] and Gao *et al.* [13] among others. There are also concerns that matrix cracks may affect electrical properties of the structural composite capacitor material. By the current structural capacitor design, with structural electrodes and a ductile polymer separator film, it is believed that cracks in the electrodes caused by high tensile strains may be sustained without substantial loss in capacitance. However, to date no experimental studies have been performed to confirm this and consequently no method to perform such measurements is available. Hence, there is a need to develop a method to evaluate the effect of matrix cracks on the electrical performance in multifunctional composite materials. In this study we propose such a method to measure capacitance of a structural composite capacitor material under tensile loading, and present the first results on structural capacitor damage tolerance with respect to its capacitance. It should be noted that the work presented here is focused on the development of the testing method for the capacitance under influence of matrix cracks and not to correlate the cracks to the change in capacitance which is a whole field of study in itself.

2. MATERIALS

The structural capacitor materials were made from the

same materials as in previous studies [10–11], using carbon fibre epoxy pre-preg woven laminas as electrodes separated by thermoplastic polyester (PET) dielectric film. The pre-preg was a 245 g/m² 2 × 2 Twill HS (3K) 0°/90° prepreg, MTM57/CF3200-42% RW, supplied by Cytec, UK, and the dielectric separator was a 50 µm thick (DuPont Mylar A), thermoplastic polyester film, supplied by Trafomo AB, Sweden.

Adhesion between PET and epoxy is generally poor and earlier studies [10–11] have proposed plasma treatment as a route for improved adhesion. In the current study NaOH was examined as a way to chemically etch the PET-film to provide better adhesion to the epoxy. A set of samples were prepared by etching the surface in 80°C NaOH solution (6.25 M) for 6 minutes according to the guideline by Huntsman for pre-treatment of PET [14]. The NaOH was supplied by Sigma Aldrich.

2.1. Composites Manufacture

Composite manufacture was done in the same manner as in previous work [7–11]. Laminates were stacked in the desired configuration, vacuum was applied followed by debulking without heat for 30 minutes, and then cured according to the supplier's recommendations (120°C for 30 minutes). A schematic of the manufacture is shown in Figure 1.

2.1.1. Specimen Preparation

Firstly, interlaminar shear strength (ILSS) specimens were manufactured to allow evaluation of the effect of the NaOH etching of the PET-film on separator adhesion to the CFRP electrode laminates. ILSS specimens were made using a lay-up of [pre-preg₁₀/PET-film/pre-preg₁₀] providing a

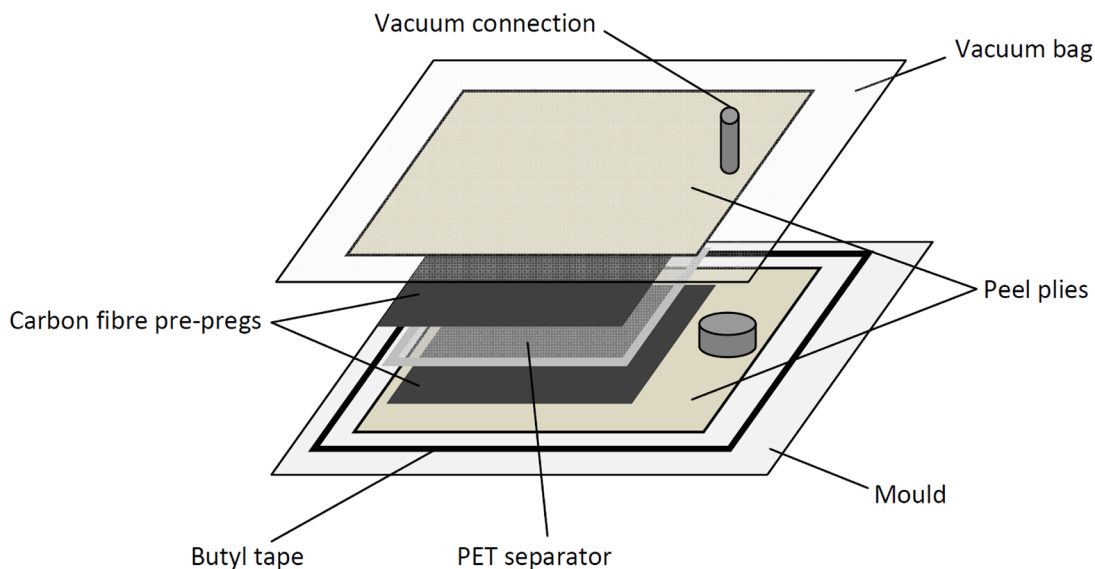


Figure 1. Schematic description of laminate manufacture.

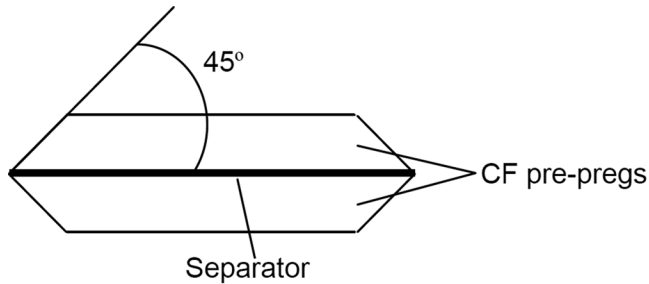


Figure 2. Principle cross-section of a tensile specimen for capacitance measurements.

thickness close to that recommended in the ASTM standard for short beam interlaminar shear strength test [15]. Nominal specimen dimensions were 30.3 mm long, 10.1 mm wide and 5.05 mm thick.

For damage tolerance studies of the multifunctional composite material tensile structural capacitor specimens were made from four prepreg plies, two on each side of the PET film. The method developed here is based on the ASTM standard for tensile testing of composites [16]. The tensile test is well suited for introducing matrix cracks in the specimen and is straightforward to perform. Since the test is not aimed at measuring stiffness or strength, but merely to introduce matrix cracks, there is no need for full length specimens as recommended in the standard [16]. For this reason specimen smaller than that recommended in the ASTM standard, 160 mm long and 20 mm wide (c.f. the length 250 mm and width 25 mm in [16]) were prepared. The chosen lay-up resulted in a theoretical nominal specimen thickness of 1.05 mm. These dimensions allow fitting of the extensometer and the electrical connections needed to perform the test. The tensile specimens were tabbed with 2 mm thick GFRP tabs bonded to the specimens with Araldite 2012 epoxy adhesive and cured overnight at room temperature. The tabs served two purposes, to provide a good grip in the tensile test machine and to electrically insulate the specimens from the tensile testing machine so as not to disturb the electrical measurement.

Specimen preparation required cutting, in this process short circuiting from carbon dust and bridging fibres at the edges was of concern. To mitigate short circuit in the specimens the edges extending parallel to the loading direction were grinded and polished in a 45° angle from the separator mid-plane, as schematically illustrated in Figure 2. A photograph of a specimen is shown in Figure 3.

A set of five specimens were made for both ILSS and tensile capacitance tests.



Figure 3. Tensile capacitance specimen.

3. EXPERIMENTAL CHARACTERISATION

3.1. Measuring Effects of NaOH Surface Treatment

The motivation for finding a good surface treatment stems from the need to achieve intralaminar matrix cracks without prior delamination at the epoxy/PET-film interface. Earlier studies using plasma treatment to improve adhesion between epoxy and the PET separator have shown onset of delamination failure around 0.2% strain [10–11]. The early delamination failure onset is a problem in this study as delaminations may form prior to intralaminar matrix cracks, and well below the targeted strain level of 0.6%. In this study, the aim was to initiate intralaminar matrix cracks only. Intralaminar matrix cracks are commonly formed as the first mode of damage in composites during service serving as initiation sites for delaminations and fibre failures. The effect of intralaminar matrix cracks on the mechanical performance is usually small [12], whereas delaminations can be critical to the mechanical performance [17]. Matrix cracks and delaminations in a multifunctional composite capacitor are schematically illustrated in Figure 4.

Interlaminar shear strength (ILSS) was measured on the structural capacitor laminates to evaluate the effect of NaOH treatment of the PET-film on its adhesion to the CFRP electrodes. The results were compared to those achieved for neat and plasma treated PETfilms reported previously [10–11]. The interlaminar shear strength was evaluated at room temperature using the short beam three-point bending test according to the ASTM D2344/D2344 M standard [15]. The equipment used was a MTS 20/M with a 10 kN load cell. A constant crosshead speed of 1 mm/min was used.

3.2. Damage Investigation

To get an insight in the amount of damage sustained by the specimens the crack density (cracks per length of specimen) was evaluated.

The angled edge used to avoid short circuit of the charged structural capacitor made it difficult to detect cracks during tensile loading. Therefore, after testing, completing a full loading-unloading cycle in tension and the capacitance

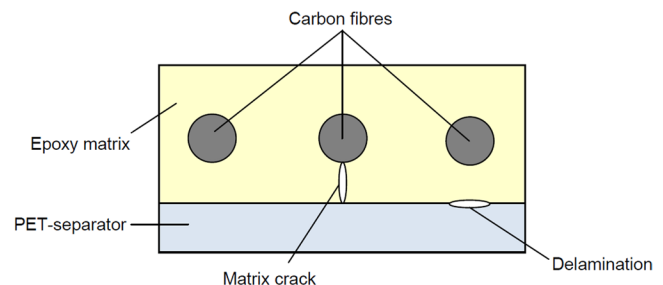


Figure 4. Schematic representation of undamaged and damaged structural capacitor composite.

measurements, the specimen's edges were grinded and polished to a 90° angle. The specimens were then fitted to the tensile tester again and loaded to a lower strain (approximately 0.3%) than before to open up the cracks making them possible to detect. A random 20 mm part of the specimen edge was chosen for close up microscopic evaluation using a portable USB microscope (Dino-Lite Pro) to determine the crack density in the specimen.

3.3. Measuring Effects of Intralaminar Matrix Cracks on Capacitance

To characterise the structural capacitor materials electrical performance the capacitance was measured by sweeping through 200 mHz–100 kHz at 1 V recording the electrical response (impedance spectroscopy). The equipment used was a Gamry Reference 3000 with Gamry Instruments Framework and Gamry Echem Analyst. A simple model for the structural capacitor material, shown in Figure 5, was used. In this model a capacitance (C) was connected in parallel with a resistance (R2) and in turn connected in series with a resistor (R1). C and R2 are connected to the PET-films electrical properties whereas R1 is connected to the electrical resistivity in the electrodes. The Echem Analyst software (Levenberg-Marquardt method) was used to find the best fit to the measured data by adjusting the parameters, R1, R2 and C.

The specimens were electrically connected to the potentiostat by thin enamelled wires and copper tape with conductive glue. This set-up is very flexible and allowed fast changes of specimen in the tensile test machine. A specimen mounted in the tensile tester is shown in Figure 6, where the extensometer has been removed for better visibility of the electrical wires. The position of the extensometer is visualised by the white areas on the surface of the specimen. Figure 7 illustrates the principle test setup.

The specimens were loaded in tension at a stroke of 1 mm/min up to 0.6–0.65% strain to introduce intralaminar matrix cracks in the structural capacitor CFRP electrodes. Matrix cracks typically occur beyond 0.2% strain [13]. Capacitance was measured before tensile loading, during tensile loading and after the load had been released. By this procedure a

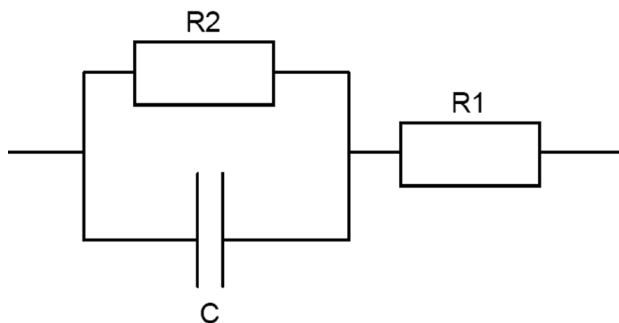


Figure 5. Structural capacitor electrical model.

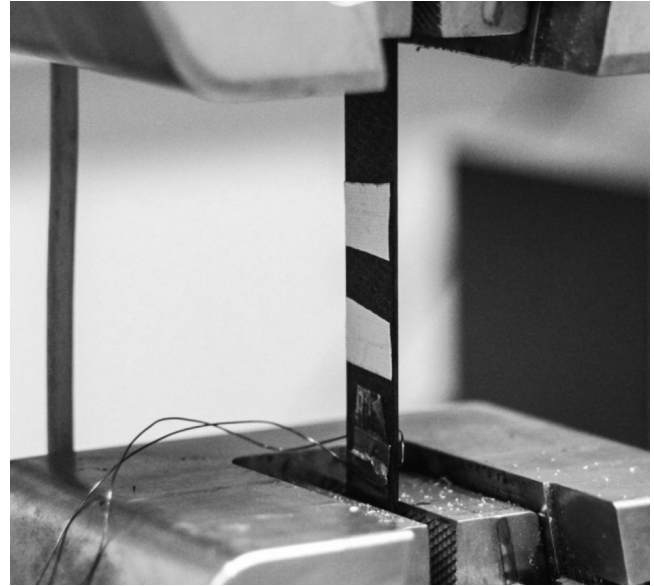


Figure 6. Specimen for measurement of capacitance with matrix cracks.

comparison of capacitance for undamaged specimens, specimens with open cracks and specimens with closed cracks was facilitated.

4. RESULTS

4.1. Effects of NaOH Surface Treatment on ILSS

Results of the effect on ILSS of NaOH treatment of the PET-film are presented in Table 1. In the Table, ILSS data for the same structural capacitor materials with plasma treated PET-film separator as well as for a full CFRP reference laminate are also presented for comparison. As seen in Table 1

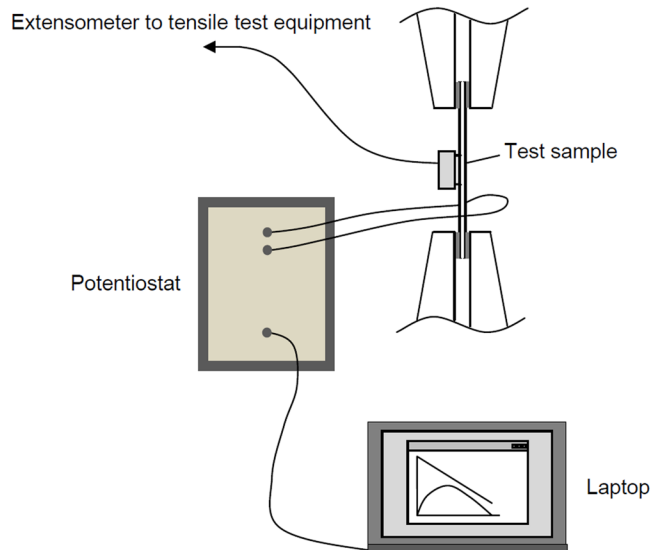


Figure 7. Principle test setup.

Table 1. ILSS for NaOH Treated, Plasma Treated Structural Capacitor Materials and a CFRP Reference.

Sample	No Treatment [11]	NaOH	Plasma Treatment [11]
PET-film 50 μm	29.5 ± 1.3	34.3 ± 0.6	29.6 ± 1.4
CFRP Ref.	54.4 ± 1.5	–	–

the plasma treated capacitor material specimens showed significantly lower ILSS values than the CFRP reference. The NaOH treatment shows a modest improvement in performance compared to the plasma treated capacitor material, but its interlaminar shear strength is still significantly lower than that of the reference. Hence, neither plasma treatment nor NaOH etching provide strong adhesion between the CFRP electrodes and the PET separator. The NaOH etching was chosen for this study as it provides the best adhesion, and hence the least risk of delaminations forming prior to intralaminar matrix cracks during the tensile loading.

4.2. Damage Characteristics

The specimens were polished flat at the edges after testing to allow identification of matrix cracks present during the test. An average crack density of 0.26 cracks/mm was found in the five specimens examined. However, it was very difficult to identify cracks due to the small crack opening displacement in the fairly thin laminates. Cracks were found to occur in all 90° bundles. In some cases the matrix cracks were found to link up to an existing pore (the out of autoclave manufacturing process resulted in some porosity of the laminates, usually found in the interface between the two plies of pre-preg). A typical pore is shown in Figure 8. Figure 9 shows typical matrix cracks, pointed out by the thin white arrows, in a specimen after testing. The middle crack is seen to link up with a pore in between the pre-preg plies. The PET separator is also clearly visible in the centre of the

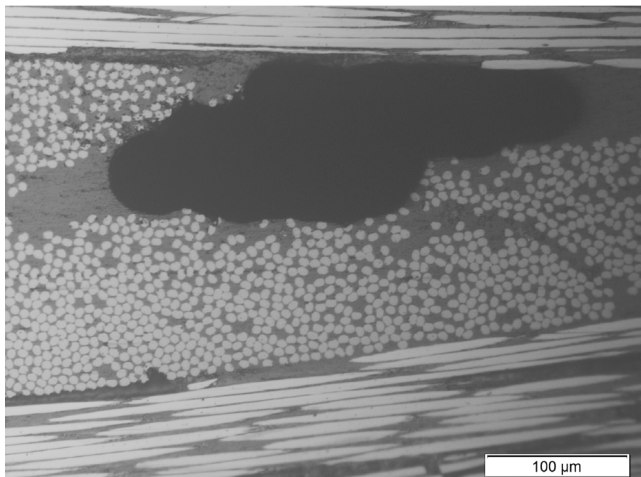


Figure 8. Close up of a typical pore inside the CFRP electrode.

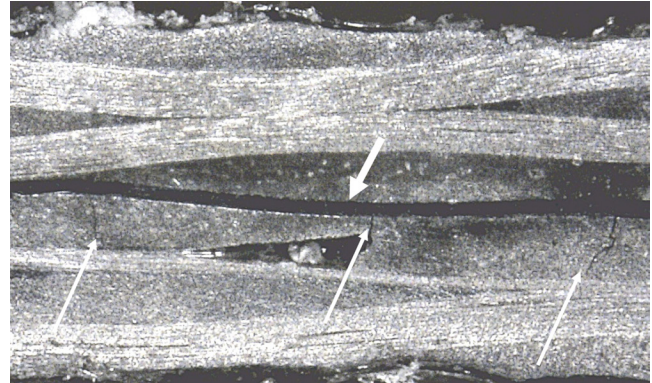


Figure 9. Matrix cracks (pointed out by thin arrows) in CFRP electrodes in a tensile capacitance specimen. The PET separator is identified by the thick arrow.

picture, extending from left to right and marked out by the thick white arrow. Figure 10 shows a close-up of a matrix crack with a white arrow indicating the location of a transverse crack in the vicinity of the PET separator film.

The crack density, and the corresponding crack opening displacement, was too small to result in any significant stiffness reduction. A stiffness reduction of approximately 0.15% was estimated for a crack density $\rho = 0.26$ cracks/mm using the approach by Varna and co-workers Lundmark [18] and Mattsson [18]. Consequently, only the effect of the presence of cracks on capacitance was evaluated experimentally.

4.3. Effect of Matrix Cracks on Capacitance

The results from the non-mechanically loaded capacitance measurements are presented in Table 2. A significant drop in capacitance for the NaOH treated film was observed compared to the non-treated and plasma-treated films. It should be noted that the geometry of the specimens measured are different for the different specimens; the non-treated and plasma treated specimens were square 100 × 100 mm

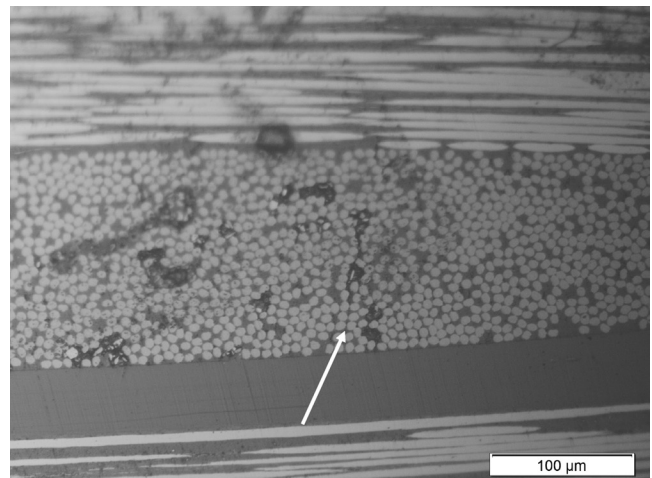


Figure 10. Close up on a matrix crack extending towards the PET separator film.

Table 2. Capacitance of the Structural Capacitors.

Dielectric	Capacitance [nF/m ²]
PET-film 50 μ m	447 \pm 3.8 [9]
PET-film 50 μ m 15s PT	442 \pm 2.6 [9]
PET-film 50 μ m NaOH	8.0 \pm 4.1

and the NaOH specimens were 160 \times 20 mm with angled edges. However, the geometric and connector type differences did not cause this significant drop in capacitance as the specimen geometry and connector was checked and found to provide capacitances of the expected level for non treated PET-film before proceeding with this study. Capacitance measurements were performed on the plates prior to cutting and specimen preparation for NaOH treated and non-treated PET capacitor. The results conclusively showed similar capacitances for plates and specimens of each kind, i.e. approximately 8 nF/m² for the NaOH treated and 440 nF/m² for the non-treated materials. Furthermore the validity of the connector was proven by consistent capacitance results for 100 \times 100 mm square specimens with copper mesh connector, plates with copper tape connector and finished 160 \times 20 mm specimens with angled edges. NaOH etching creates a porous and rough surface [20] and for a thin film like the one used in this study this may affect the resistive properties of the whole film resulting in a lower dielectric constant. The rough surface provides better wetting and adhesion of the epoxy matrix in the electrodes which can result in a larger amount of epoxy at the electrode/separator interface effectively creating a thicker separator layer further reducing capacitance. However no general thickness increase by the formation of resin rich interface layers between the CFRP electrodes and the PET separator could be recorded by microscopy of polished samples. The drop in capacitance, caused by the NaOH treatment, does not cause a problem for the purpose of this study, where the change in capacitance from the formation of matrix cracks is sought. However, for realisation of structural capacitor materials of this design the NaOH etching of the PET-film is not advised.

The results from the capacitance measurements in the tensile test machine are shown in Table 3. As seen there was a significant drop, but not critical, in capacitance for the tensile loaded state (i.e. at 0.6% strain). This is found inherent to the opening of matrix cracks resulting in a lower dielectric constant for the insulating layer (consisting of the PET-Film and the epoxy matrix that sits in between the CF electrodes) since air has a lower dielectric constant than polymers. No

Table 3. Capacitance Change with Matrix Cracks.

Dielectric	Capacitance nF/m ²		
	Before	Loaded	After
NaOH treated 50 μ m PET	8.0 \pm 4.1	3.9 \pm 1.3	11.0 \pm 3.0

other damage mechanisms, i.e fibre fractures or delaminations, were observed to occur in the tests. It should be noted that as the specimen was unloaded the capacitance was recovered, and was even higher than that before the mechanical load had been applied. The recovery was found inherent to complete crack closure as the specimens were unloaded (i.e. the small crack opening displacement observed in loaded specimens was found to vanish as cracks closed completely when the specimens were unloaded). A possible explanation for the gained capacitance is permanent plastic deformation of the insulating layer consisting of the PET-film and epoxy matrix resulting in a thinner separator after unloading than before introduction of matrix cracks. However this assumption has not been possible to confirm through inspection in an optical microscope.

The most important result is the fact that the capacitance of the structural capacitor is not critically affected by mechanical damage in the structure.

5. CONCLUSIONS

In this study a method to investigate the effect of intralaminar matrix cracking on capacitance of structural capacitors has been developed and employed. The method developed for measuring capacitance with matrix cracks works very well and the use of simple specimen geometry, in a tensile test set-up, along with a versatile potentiostat makes the test applicable on other types of multifunctional composite devices, i.e. supercapacitors or batteries.

The structural capacitors developed and tested in this study were found to maintain their capacitance even after sustaining intralaminar matrix cracking in the CFRP electrodes all the way up to the PET separator. This result is very important as the material shows a significant robustness to perform its electrical function in a damaged state.

Further, the effects of different surface treatment on the separator have been studied. NaOH treatment performed in this study has been compared to the plasma treatment performed in earlier studies [7–11] and it has been shown that NaOH is not suitable as surface treatment for the PET-film in a multifunctional composite capacitor. The treatment will improve the adhesion to epoxy but it will simultaneously lower the capacitance of the device to an unacceptable level.

6. ACKNOWLEDGEMENTS

Financial support from the European Commission via the FP7 project grant no. 234236, StorAge is gratefully acknowledged. Mr. P. Bartolotta is gratefully acknowledged for his assistance with NaOH treatment, and mechanical testing. Mr. M. Loukil is gratefully acknowledged for his assistance with some microscopy work. Prof. J. Varna is gratefully acknowledged for his participation in valuable discussions.

7. REFERENCES

- [1] Chung DDL, Wang S. Carbon fiber polymer-matrix structural composite as a semiconductor and concept of optoelectronic and electric devices made from it. *Smart Matererials and Structures*, Vol. 8, p. 161–166, 1999. <http://dx.doi.org/10.1088/0964-1726/8/1/018>
- [2] Luo X, Chung DDL. Carbon-fiber/polymer-matrix compositors as capacitors. *Composite Science and Technology*, Vol. 61, p. 885–888, 2001. [http://dx.doi.org/10.1016/S0266-3538\(00\)00166-4](http://dx.doi.org/10.1016/S0266-3538(00)00166-4)
- [3] Baechle DM, O'Brien DJ, Wetzel ED. Design and processing of structural composite capacitors. *Proceedings of SAMPE 2007*, Baltimore, MD, USA, 2007.
- [4] O'Brien DJ, Baechle DM, Wetzel ED. Multifunctional structural composite capacitors for U.S. army applications. *Proceedings of SAMPE 2006*, Dallas, Texas, USA, 2006.
- [5] Wetzel ED. Reducing weight: Multifunctional composites integrate power, communications and structure, *AMPTIAC Quarterly*, Vol. 8, p. 91–95 2004.
- [6] Yurchak OB, O'Brien DJ, Baechle DM, Wetzel ED. Shear properties of multifunctional structural capacitors *Proceedings of SAMPE 2012*, Baltimore, MD, USA, 2012.
- [7] Carlson T, Ordéus D, Wysocki M. "Load carrying composites for electrical energy storage" SICOMP TR08-02, Swerea SICOMP, Sweden, 2008.
- [8] Carlson T, Ordéus D, Wysocki M, Asp LE. Structural capacitor materials made from carbon fibre epoxy composites, *Composite Science and Technology*, Vol. 70(7), p.1135–1140, 2010. <http://dx.doi.org/10.1016/j.compscitech.2010.02.028>
- [9] Carlson T, Ordéus D, Wysocki M, Asp LE. CFRP structural capacitor materials for automotive applications, *Plastics, Rubbers and Composites*, Vol. 40(6-7), p. 311316, 2011.
- [10] Carlson T, Asp LE. Structural carbon fibre composite/PET capacitors—Effects of dielectric separator thickness, *Composites Part B: Engineering*, Vol 49, p. 16–21, 2013. <http://dx.doi.org/10.1016/j.compositesb.2013.01.009>
- [11] Carlson T, Asp LE. Plasma treatment—a route for improved adhesion between PET and epoxy in multifunctional composite capacitors, *Proceedings of ECCM15* Venice, Italy, 2012.
- [12] Varna J, Talreja R. Integration of macro- and microdamage mechanics for performance evaluation of composite materials, *Mechanics of Composite Materials*, Vol. 48(2), p. 145–160, 2012. <http://dx.doi.org/10.1007/s11029-012-9261-y>
- [13] Gao F, Boniface L, Ogin SL, Smith PA, Greaves RP. Damage accumulation in woven-fabric CFRP laminates under tensile loading: part 1. Observation of damage accumulation, *Composites Science and Technology*, Vol. 59, p. 123–136, 1999. [http://dx.doi.org/10.1016/S0266-3538\(97\)00231-5](http://dx.doi.org/10.1016/S0266-3538(97)00231-5)
- [14] Surface preparation and pretreatments, www.huntsman.com/adhesives, 2010.
- [15] ASTM Standard test method for short-beam strength of polymer matrix composite materials and their laminates, *Annual book of ASTM standards*, West Conshohocken, Vol. 15.03, p. 71–78, 2010.
- [16] ASTM Standard test method for tensile properties of polymer matrix composite materials and their laminates, *Annual book of ASTM standards*, West Conshohocken, Vol. 15.03, p. 79–91, 2010.
- [17] Asp LE, Nilsson S, Singh S, An experimental investigation of the influence of delamination growth on the residual strength of impacted laminates, *Composites Part A: Applied Science and Manufacturing*, 2001;32(9):1229–1235. [http://dx.doi.org/10.1016/S1359-835X\(01\)00075-6](http://dx.doi.org/10.1016/S1359-835X(01)00075-6)
- [18] Lundmark P. and Varna J., "Constitutive Relationships for Laminates with Ply Cracks in In-plane Loading", *International Journal of Damage Mechanics*, Vol. 14(3), p. 235–261, 2005. <http://dx.doi.org/10.1177/1056789505050355>
- [19] Mattsson H.D. and J. Varna, Average strain in fiber bundles and its effect on NCF composite stiffness, *J. of Engineering materials and technology*, 129, p. 211–219, April 2007.
- [20] Garbassi F, Morra M, Occhiello E. *Polymer Surfaces—From Physics to Technology*, Revised and updated edition, p. 365, 1998.



Experimental Assessment of Single and Cumulative Impact Damage in Carbon Fiber Polymer Matrix Composites Using Electrical Resistance Measurements

JUSTIN McANDREW and OLESYA I. ZHUPANSKA*

Department of Mechanical and Industrial Engineering The University of Iowa, Iowa City, IA 52242

KEYWORDS

carbon fiber
polymer matrix composites
impact damage
electrical resistance
damage sensing

ABSTRACT

In this work the impact damage sensing capabilities in AS4/3501-6 carbon fiber polymer matrix composites are investigated. A fully instrumented experimental setup for characterization of electrical properties has been developed. The one-dimensional electrical resistance method was employed for damage sensing. 16-ply [0/45/–45/90]_{2S} and 32-ply [0/45/–45/90]_{4S} laminates were tested. Single impact and cumulative low velocity impact studies were conducted and electrical resistance measurements were performed to assess damage. The results show that the one-dimensional electrical resistance technique had a limited success at sensing impact damage in AS4/3501-6 composites due to low initial resistances of the composites tested.

© 2014 DEStech Publications, Inc. All rights reserved.

1. INTRODUCTION

Damage in composites due to impact represents a serious design concern for use of advanced carbon fiber reinforced polymer (CFRP) composite materials as structural elements in aerospace applications. As current and future aerospace systems rely more and more on fiber-reinforced polymer composites, damage detection becomes increasingly important and non-destructive evaluation methods are still highly desirable for such composites. At the same time, adding damage sensing functionality to composites represents an attractive alternative, where a composite material itself may serve as a damage sensor. In addition, integration of load bearing and sensing capabilities will lead to the realization of the concept multifunctionality where composite structures possess not only superior mechanical characteristics, but also other concurrent functional capabilities.

There have been a number of studies on the electrical characterization of carbon fiber polymer matrix composites conducted in the past [1–13] that attempted to monitor changes in the electrical resistance and electric field that oc-

cur as a result of mechanical damage. Two main techniques have been employed to sense impact damage: the potential method and the resistance method. Both techniques involve the application of two electrodes to send current and any number of electrodes to measure voltage. The difference between the methods lies in the direction of the potential measurement. In the resistance method, the applied current line and the electric potential line coincide, whereas in the potential method, they do not [4,13]. To sense the damage distribution, the one-dimensional resistance method is adequate. To determine the location of the damage, a two-dimensional method is required. The two-dimensional resistance method requires a large array of contacts covering the surface, with the left and right edge contacts used for current application and the inner contacts used for voltage measurement. Due to the number of contacts involved, and the fact that they cover the entire surface, the two-dimensional resistance method is impractical. The one-dimensional potential method avoids these shortcomings since it can be employed using only contacts along the edges of the specimen. One pair of the contacts is used for applying current, while voltage is measured at all of the other contacts [5].

Four different resistances can be measured using the one-dimensional resistance method: the top surface, the bottom

*Corresponding author. E-mail: olesya-zhupanska@uiowa.edu;
Tel: +1-319-335-5678; Fax: +1-319-335-5669

surface, the through-thickness, and the oblique (i.e. through the thickness of the specimen at an oblique angle). The surface resistance is effective at sensing fiber breakage, while the through-thickness resistance is responsive to delamination. The oblique resistance is sensitive to both types of damage [5]. Since the lay-up, thickness, and the ply-count of a specimen will influence the type of impact damage it sustains, so too will these variables dictate which resistance measurement is appropriate. For example, for thick laminates consisting more than 16 plies, both the through-thickness and the oblique resistance are recommended, since interior damage is the primary damage type for such specimens. Overall, the oblique resistance is recommended, as it is effective for all laminate lay-ups and thicknesses, in addition to being able to sense both minor and major damage [6].

Various types of investigations have been conducted using the one-dimensional resistance method and the aforementioned resistance types. The ability to detect impact damage via electrical resistance measurement was compared to the more traditional ultrasonic detection method in [7]. Three types of resistance were measured: the top, bottom, and oblique. For a 24-ply quasi-isotropic specimen, the oblique resistance was found to be the most dependable damage indicator since it increased monotonically with impact energy. This was not always the case for the top and bottom surface resistances. The surface resistances varied significantly between the three tested sections, as the surfaces were affected greatly by impact. The opposite occurred with the oblique resistance data since it represents the interior damage. It was determined that electrical resistance measurement was a more sensitive damage inspection method than ultrasonic inspection, due in part to the significant amount of noise associated with the latter method.

Sensing of damage at a point removed from the impact region via both electrical resistance and potential measurement was investigated in [8]. Two types of four-probe resistance were measured, namely the through-thickness and the oblique. The through-thickness resistance was more sensitive than the oblique resistance, since the primary damage mode encountered was delamination. Although the through-thickness resistance was more sensitive, the oblique resistance exhibited more advantages. For example, the oblique resistance was more suitable for sensing the damage in the impact region at a position removed from the region. In addition, due to the contact scheme, it was impossible to measure the resistance at the impact region using the through-thickness method.

The sensitivity of the one-dimensional resistance method was compared with that of the two-dimensional potential/resistance method in [9]. For the two-dimensional potential method, it was shown that the most sensitive results for major damage were obtained when the potential line was as close as possible to the point of impact. For minor damage, it was shown that the most sensitive results were obtained

when the potential line was as close as possible to the current line. When the potential line was directly on top of the current line, thus representing the resistance method, the highest degree of sensitivity was attained. Thus the resistance measurement was found to be more sensitive than the potential gradient measurement in the two-dimensional potential/resistance method. When compared with other work, however, the two-dimensional potential/resistance method was much less sensitive than the one-dimensional resistance method. This is a consequence of current spreading that occurs between the two current contacts in the two-dimensional potential/resistance method, which decreases sensitivity.

In most of the damage sensing via the one-dimensional resistance method research, narrow specimens with widths of 10 or 12 mm have been used [4,6–8,11,12]. Such specimen widths have been used to obtain large resistance measurements and high sensitivity. However, such specimens prevent the use of standard low velocity impact test fixtures, such as the NASA fixture outlined in NASA RP-1092 [14]. Thus one of the objectives of the current work was to determine if low velocity impact damage could be sensed using a standard test fixture and specimens with more practical dimensions.

2. EXPERIMENTAL METHODS

A four-probe method for electrical resistance measurements was used in the presented work. In the four-probe method, the electrical resistance is measured with four electrical contacts, where an electric current passes through two outer contact and two inner contacts are used for voltage measurements. Figure 1 illustrates the four-probe method

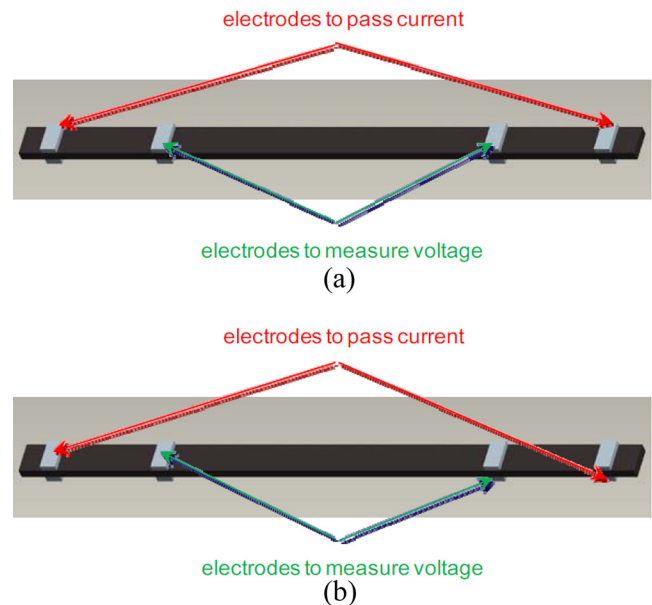


Figure 1. Four probe resistance measurements; (a) top resistance measurement and (b) oblique resistance measurement.

for measurements of top surface and oblique (i.e. through the thickness of the specimen at an oblique angle) resistance that was employed in this work. In such a way, the electrical contact resistance at voltage contacts does not contribute to the resistance of the part of the specimen between the voltage contacts, which leads to more accurate and consistent measurements. In contrast, a two-probe method that utilizes only two contacts for both current applications and voltage measurements has been found very sensitive to the contact conditions between electrodes and a specimen. Moreover, most of the resistance measured using a two-probe technique is attributed to the contact resistance but not the specimen resistance.

AS4/3501-6 composite laminate were used in the presented work. Two types of laminates were tested: a 16-ply orthotropic $[0/45/-45/90]_{2s}$ laminate (thickness = 2.25 mm) and a 32-ply orthotropic $[0/45/-45/90]_{4s}$ laminate (thickness = 4.5 mm). Square specimens were cut with a nominal side length of 15.24 cm.

Four electrodes, in the form of straightened 22 AWG copper wire with lengths of approximately 20.5 cm, were painted on both the top and bottom surfaces of the specimens using SPI Conductive Silver Paint (Structure Probe, Inc., SPI# 05002-AB). These electrodes extended across the entire surfaces of the specimens. The excess length of the electrodes on the top surface extended off the bottom edge of that surface, while that of the electrodes on the bottom surface extended off the top edge of that surface. Prior to painting, the surfaces of the composite were sanded directly underneath the locations of the electrodes using 600 grit sand paper. The electrodes were spaced 30 mm apart, centered about the composite centerline. This spacing scheme, suggested in [10], was used to obtain both high spatial resolution and sensitivity. Contrary to much of the published work, however, the electrodes were placed parallel to the surface fiber directions. Preliminary work using electrodes placed perpendicular to the surface fiber directions with the same spacing proved problematic. At low impact energies, the change between two resistance measurements was within the error of measurements, while at higher impact energies the electrodes came off the bottom surface due to damage. After the silver paint had dried, a layer of epoxy (Hysol® E-120HP, LOCTITE® P/N 29353) was applied to the electrodes to maintain structural integrity during impact. An example of a completed specimen with electrodes attached is shown in Figure 2.

To impact the specimens, an Instron Dynatup Model 8200 Drop Weight Impact Testing Instrument was used. The impact machine was outfitted with a 1.27 cm (1/2 in) diameter hemispherical tup insert (Model 8914-1, Instron P/N 7910-216). The mass of the drop-weight assembly was 6.1656 kg. To clamp the specimens during impact, a NASA test fixture was used. To allot for the surface electrodes on the specimens, two custom fixture plates were designed for

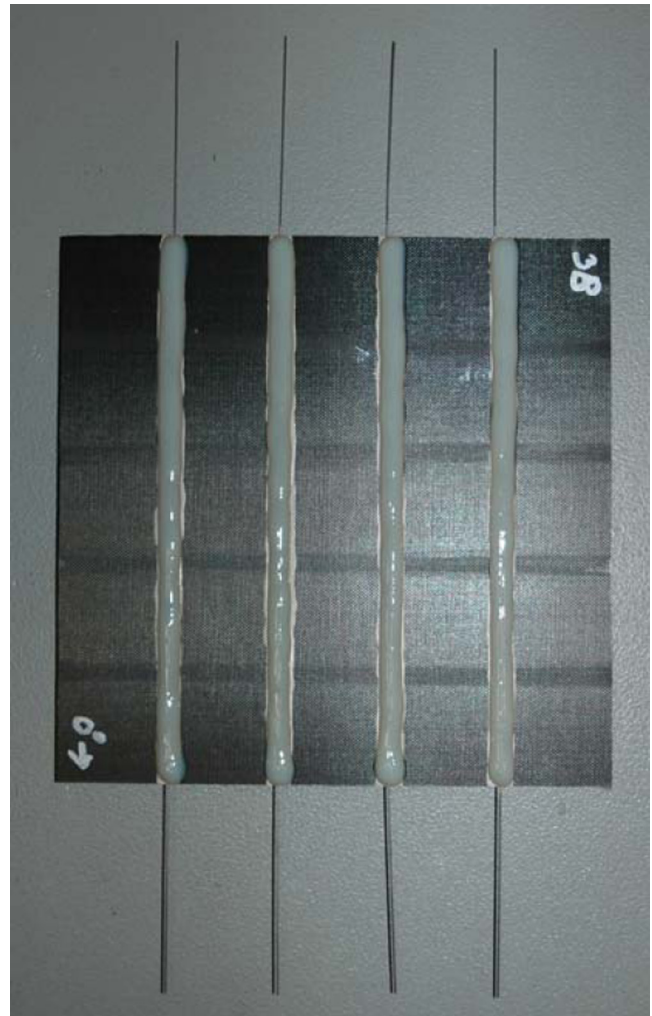


Figure 2. Example of a completed specimen with electrodes attached.

use in conjunction with the NASA test fixture. These plates, made from sheet PVC, had dimensions similar to the NASA test fixture base and top plate but with channels to account for the electrodes.

Before and after impact, the top surface resistance and the oblique resistance of the impact region was measured using the four-probe method. An Agilent model number 34420A nanovolt/micro-ohm meter was employed to make the measurements. To supply the necessary channels, the micro-ohm meter was connected to a 20 channel Agilent 34901A multiplexer card. The channels on the card were opened and closed using an Agilent 34970A switch unit. To connect to the specimens, test leads were made from twisted, shielded pair cable (two pair, 22 AWG stranded copper) (General Cable, Carol Brand P/N C1352.12.10) and alligator clips. Figure 3 shows a complete experimental setup.

Prior to performing impact tests, the initial resistance values for every specimen were recorded. Figure 4 shows the top and oblique resistance values for the 16-ply specimens,

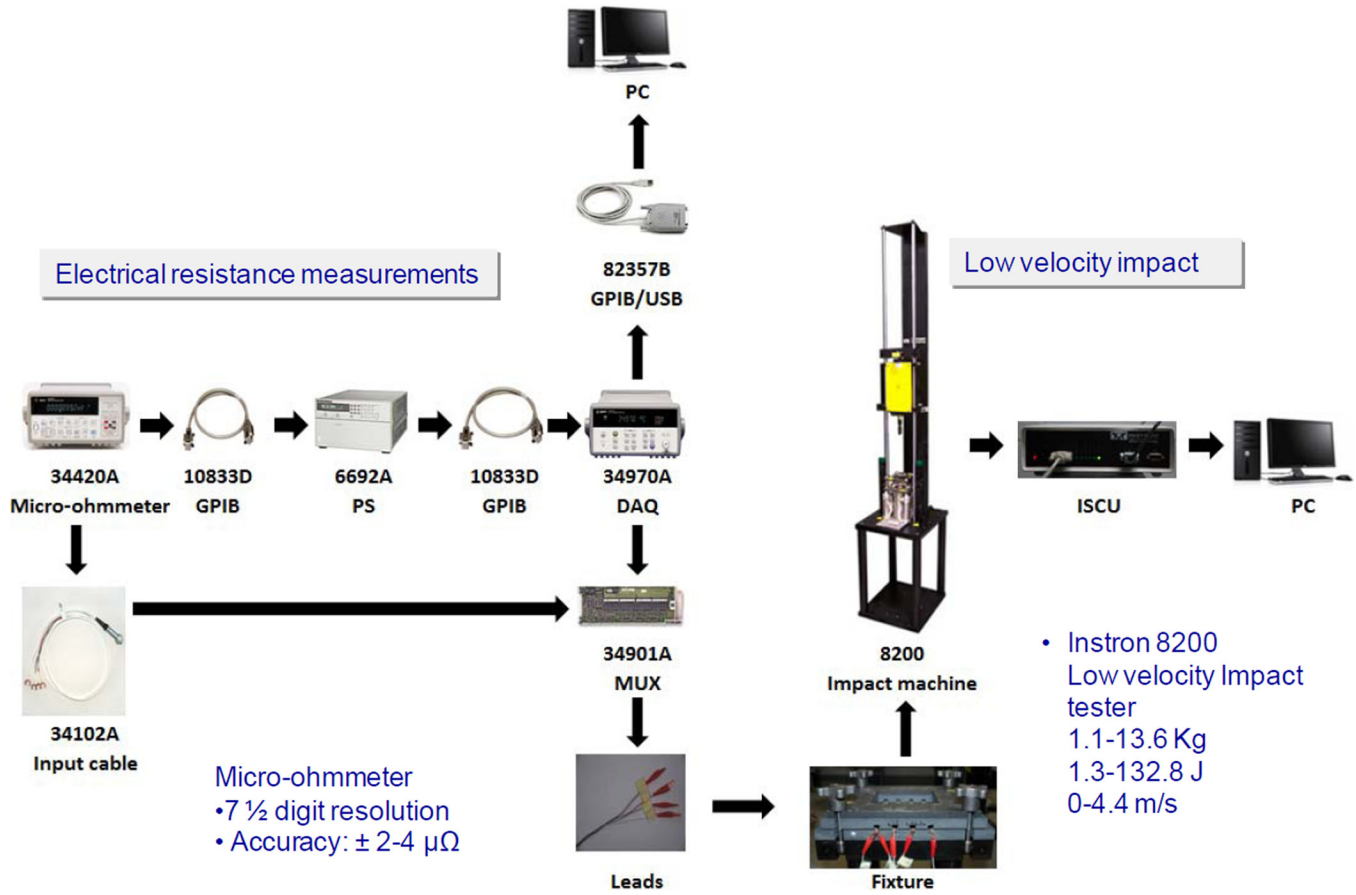


Figure 3. Experimental setup.

while Figure 5 shows the respective resistance values for the 32-ply specimens used in this study.

Three different impact energy levels were tested for both the 16-ply and 32-ply specimens. For the 16-ply specimens, the energy levels were 7.19 J, 8.67 J, and 10.23 J, while for the 32-ply specimens, the energy levels were 19.91 J, 23.02 J, and 27.16 J. The “lowest”, “intermediate”, and “highest” energy levels were chosen in such a way so as to produce visibly different damage zones. Figure 6 illustrates

damage size in three 32-ply specimens impacted at the lowest, 19.91 J, intermediate, 23.02 J, and highest, 27.61 J energy levels.

Three to five specimens were impacted at each energy level a single time. Cumulative damage was also studied by impacting a portion of the specimens (at least three) impacted once at a given impact energy multiple times, at that same energy. Due to the extensive damage caused by the highest impact energies for both ply counts, cumulative damage test-

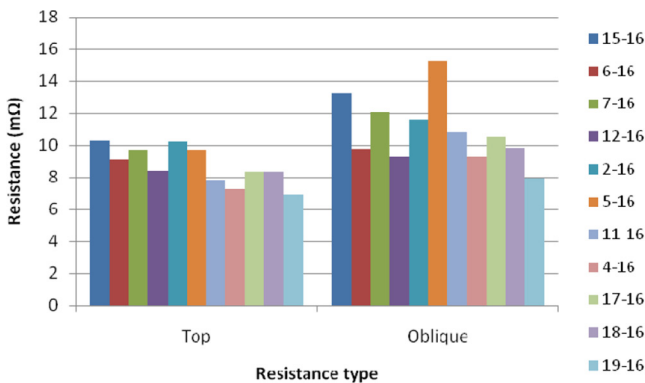


Figure 4. Initial (prior to impact) resistance values of 16-ply specimens.

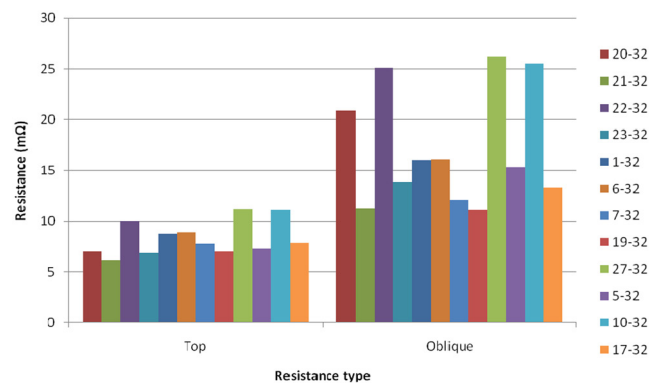


Figure 5. Initial (prior to impact) resistance values of 32-ply specimens.

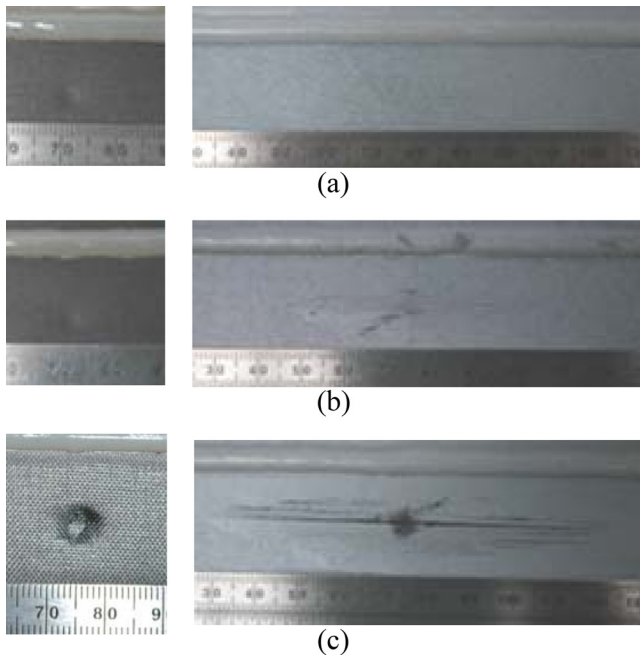


Figure 6. Top (images on the left) and bottom (images on the right) surface damage produced in 32-ply specimens impacted at three different energy levels; (a) Specimen 20-32 after impact at the lowest energy (19.91 J); (b) Specimen 7-32 after impact at the intermediate energy (23.02 J) and (c) Specimen 5-32 after impact at the highest energy (27.61).

ing was performed only at the two lowest energies for both the 16- and 32-ply specimens. The cumulative damage test specimens were impacted until they were nearly perforated. Naturally the number of impacts depended on the ply-count and energy level. For the 16-ply specimens of the 7.19 J cumulative damage study, the specimens were impacted five times, while those of the 8.67 J cumulative damage study were impacted three times. For the 32-ply specimens of the 19.91 J cumulative damage study, the specimens were impacted three times, while those of the 23.02 J cumulative damage study were impacted two times.

3. RESULTS AND DISCUSSION

3.1. Single Impact Studies of the 16-Ply Laminates

Impact of 16-ply specimens at the lowest impact energy (7.19 J) left a faint and shallow dent on the top surface and delamination at the bottom surface. A dent representative of those left on most of the specimens is shown in Figure 7, which shows the top and bottom surfaces of specimen 6-16 (the first number indicates the specimen number while the number after the hyphen indicates the ply count).

The change in resistance results for the 16-ply laminates (specimens 15-16, 6-16, 7-16, and 12-16) impacted at 7.19 J was small. For instance, specimen 6-16 experienced an increase of $0.09 \pm 0.06\%$ while specimen 12-16 experi-

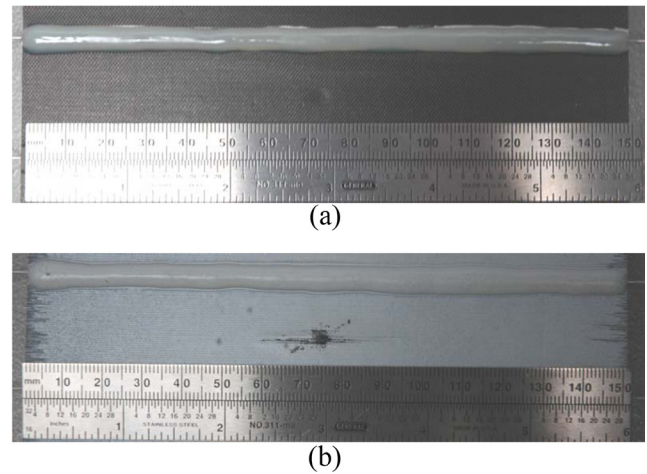


Figure 7. Specimen 6-16 after impact at the lowest energy (7.19 J); (a) top surface and (b) bottom surface.

enced a decrease of $0.63 \pm 0.07\%$. While specimen 12-16 experienced the least top surface damage of the four specimens, the detectable decrease in resistance was an unexpected result, as the resistance ideally should increase with damage. Perhaps the dent for specimen 12-16 was too shallow to break any of the fibers. Instead, more of the fibers may have come into contact after damage, creating additional pathways for the current to flow. These additional pathways may have made it easier for the current to flow across the specimen, thereby decreasing the resistance. The oblique resistance proved to be more sensitive than the top surface resistance at 7.19 J. All of the specimens experienced a change in resistance that was detectable. Arranged in decreasing magnitude, the percent changes in oblique resistance were as follows: $0.17 \pm 0.06\%$ (specimen 6-16), $0.11 \pm 0.04\%$ (specimen 15-16), $0.10 \pm 0.05\%$ (specimen 7-16), and $-0.51 \pm 0.06\%$ (specimen 12-16). Note that the first three percent changes of the previous list overlap, and thus the oblique resistance was unable to distinguish between the damage sustained by those specimens. This was an expected result, however, since the damage experienced in those specimens was fairly similar. For the lone specimen that displayed significantly different damage (specimen 12-16, which experienced the least bottom surface damage), the oblique resistance measurement produced a detectable percent change of -0.51% . This is similar in sign and magnitude to the percent change the specimen experienced in its top surface resistance measurement (-0.63%).

Impact at the intermediate impact energy (8.67 J) left in 16-ply specimens a larger, deeper, and more defined dent than those resulting from the lowest energy (7.19 J). In addition, the dents contained a v-shaped crease within them. The average dent diameter was 7.19 mm. This average is approximately 80 percent greater than that obtained from the specimens impacted at the lowest impact energy. On the bottom surface, more extensive damage was seen than



Figure 8. Bottom surface of specimen 5-16 after impact at the intermediate energy (8.67 J).

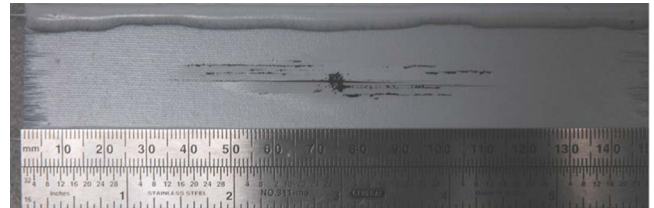


Figure 10. Bottom surface of specimen 19-16 after impact at the highest energy (10.23 J).

for the specimens impacted at the lowest energy (see Figure 8).

The change in resistance results proved to be better for the 16-ply laminates impacted at 8.67 J, as shown in Figure 9. The top surface resistance experienced a detectable increase after impact for all three specimens. Specimens 2-16, 5-16, and 11-16 exhibited percent increases of $0.24 \pm 0.06\%$, $0.25 \pm 0.14\%$, and $0.80 \pm 0.05\%$, respectively. Note that while the percent increases for specimens 2-16 and 5-16 are within accuracy of each other, the percent increase for specimen 11-16 is significantly larger. These findings correlate well with the observations made with respect to the top surface damage; namely, that specimen 2-16 and 5-16 experienced similar top surface damage while specimen 11-16 sustained the most damage. Even though the top surface resistance produced results in accordance with the damage evaluation, the oblique resistance once again proved to be more sensitive. Two of the specimens (2-16 and 11-16) experienced larger increases in oblique resistance than they did in top surface resistance, while the comparison was indeterminate for specimen 5-16. Specimen 2-16 experienced an increase in oblique resistance of $0.54 \pm 0.05\%$, specimen 5-16 an increase of $0.40 \pm 0.04\%$, and specimen 11-16 an increase of $1.11 \pm 0.05\%$. Excluding the uncertainties, these percent increases are anywhere from 1.4 to 2.3 times as large as their top surface counterparts. The percent increases for the oblique resistance also follow the same trend as those for the top surface resistance. That is, the specimen with the greatest bottom surface damage (11-16) experienced the greatest percent increase in resistance.

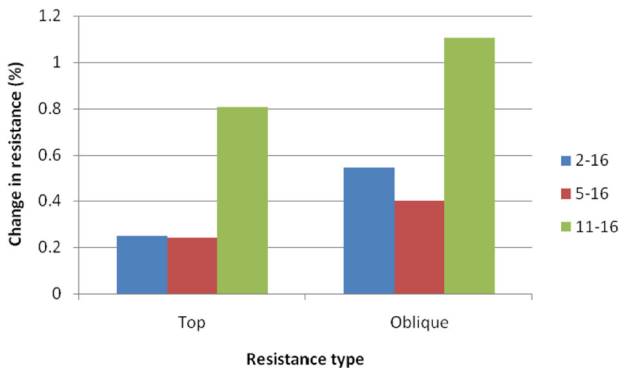


Figure 9. Percent change in resistance for the 16-ply specimens impacted at 8.67 J.

The impacts of 16-ply specimens at the highest energy (10.23 J) left even larger dents than those resulting from the intermediate energy (8.67 J). As on the top surface, more extensive damage was seen on the bottom surface of the specimens impacted at the highest energy than on those impacted at the intermediate energy. However the increase in damage was not as significant as the increase seen when comparing the specimens from the lowest and intermediate energies (see Figure 10).

The change in resistance results for the 16-ply laminates impacted at 10.23 J, shown in Figure 11, were somewhat unexpected. For specimens 4-16, 17-16, 18-16, and 19-16, the percent changes in top surface resistance were $0.32 \pm 0.06\%$, $0.50 \pm 0.22\%$, $0.36 \pm 0.05\%$, and $0.29 \pm 0.06\%$, respectively.

For the same specimen listing, the following percent changes in oblique resistance were measured: $0.25 \pm 0.06\%$, $0.53 \pm 0.05\%$, $0.44 \pm 0.06\%$, and $0.34 \pm 0.07\%$. When these percent changes and their associated uncertainties are compared with those of the top surface resistance for the same specimen, the percent changes overlap. Hence, neither of the two resistance types was more sensitive than the other in any of the four specimens, a result contrary to the findings of the 7.19 J and 8.67 J impacts.

A more profound result was obtained by comparing the results of the 8.67 J and 10.23 J impact studies. The percent changes recorded for the 10.23 J impacts were not greater than those measured for the 8.67 J impacts. For the percent changes in top surface resistance, almost all of the changes measured for the 10.23 J specimen lot overlap with those of specimens 2-16 and 5-16 ($0.24 \pm 0.06\%$ and $0.25 \pm 0.14\%$,

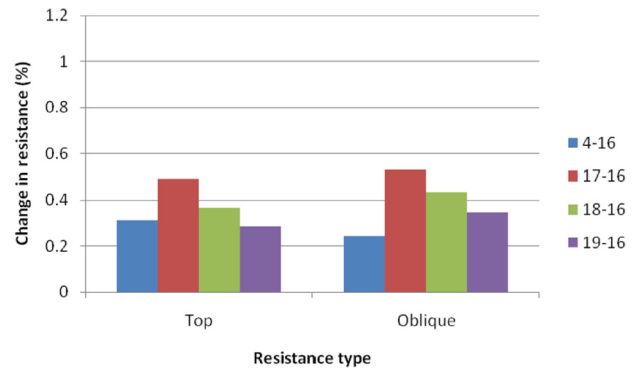


Figure 11. Percent change in resistance for the 16-ply specimens impacted at 10.23 J.

respectively) of the 8.67 J specimen lot. In addition, specimen 11-16 of the 8.67 J specimen lot experienced a much greater percent change in top surface resistance ($0.80 \pm 0.05\%$) than any of the specimens of the 10.23 J specimen lot. Similar results can be found for the percent changes in oblique resistance by comparing the 8.67 J and 10.23 J specimen lots. Specimens 2-16 and 5-16 of the 8.67 J specimen lot experienced percent changes in oblique resistance ($54 \pm 0.05\%$ and $0.40 \pm 0.04\%$, respectively) that overlapped with those of four of the five specimens from the 10.23 J specimen lot (the changes were greater than that measured for specimen 4-16). In addition, specimen 11-16 experienced a change in oblique resistance ($1.11 \pm 0.05\%$) that was much greater than any of those experienced by the specimens of the 10.23 J specimen lot. One possible explanation for the lack of a correlation between impact energy and percent change in resistance is the large variation that was present in the initial resistance values recorded. However, variation cannot entirely explain the problem, since specimens from the 8.67 J and 10.23 J specimen lots with similar initial resistances showed the same results. A better explanation, at least for the top surface results, is that sending current perpendicular to the surface fiber direction is an ineffective method of sensing top surface damage. It is believed that this ineffectiveness is caused by the way in which the current traverses the top surface when applied perpendicular to the fibers. When applied perpendicular to the fibers, the only locations in which the current can travel across the specimen are at points where adjacent fibers touch. If fibers at the impact region break during impact, this may or may not affect the resistance for current applied perpendicular to the fibers. It would only affect the resistance if the fibers at the impact region were touching before impact, and their breakage made it more difficult for the current to travel across the top surface. It is not clear what effect the direction of the applied current has on the sensing capability of the oblique resistance, since current travel is much more complicated for this resistance type. The ineffectiveness found for the oblique resistance may just be the result of the large specimen size and its associated low resistance values.

3.2. Single Impact Studies of the 32-Ply Laminates

Impact at 19.91 J impact energy left a circular dent on the top surface of the tested 32-ply specimens. The average dent diameter was 3.85 mm. On the bottom surface, minor delamination occurred for all specimens. After the impact of four 32-ply specimens at 19.91 J, the initial resistance values experienced the percent changes shown in Figure 12. For the top surface resistance, specimens 20-32 and 23-32 experienced changes too insignificant to be detectable by the measurement system. For both specimens, the initial resistance and its uncertainty overlap with the after-impact measurement and its uncertainty. Positive percent increases

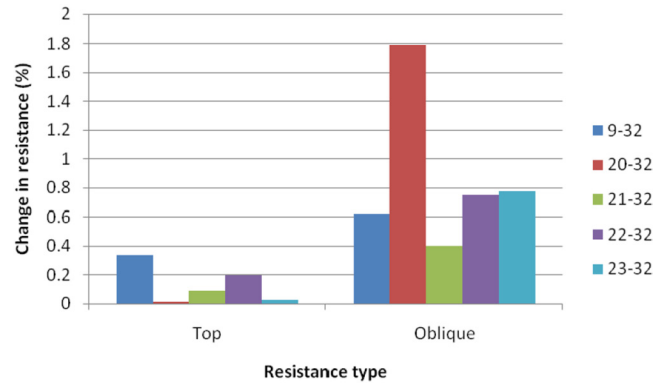


Figure 12. Percent change in resistance for the 32-ply specimens impacted at 19.91 J.

in top surface resistance were detected in all of the other specimens. Specimens 9-32, 21-32, and 22-32 exhibited percent increases of $0.33 \pm 0.08\%$, $0.10 \pm 0.07\%$, and $0.20 \pm 0.04\%$, respectively. As was the case for the 7.19 J and 8.67 J impacts of the 16-ply specimens, the oblique resistance proved to be more sensitive than the top surface resistance. All of the specimens experienced a change in oblique resistance that was detectable, and in each specimen the percent change in oblique resistance was greater than that for the top resistance. Arranged in decreasing magnitude, the percent changes in oblique resistance were as follows: $1.79 \pm .03\%$ (specimen 20-32), $0.78 \pm 0.04\%$ (specimen 23-32), $0.75 \pm 0.02\%$ (specimen 22-32), $0.62 \pm 0.06\%$ (specimen 9-32), and $0.40 \pm 0.05\%$ (specimen 21-32).

Damage on the top surface of the 32-ply specimens impacted at 23.02 J impact energy consisted of a dent that was either circular or contained a circular region in its center. The average dent diameter was 4.77 mm, or about 24 percent greater than the 3.85 mm calculated from the specimens impacted at the lower (19.91 J) energy. On the bottom surface, more extensive damage was seen than for the specimens impacted at the lowest energy.

The change in resistance results for the 32-ply laminates impacted at 23.02 J are shown in Figure 13. For the top sur-

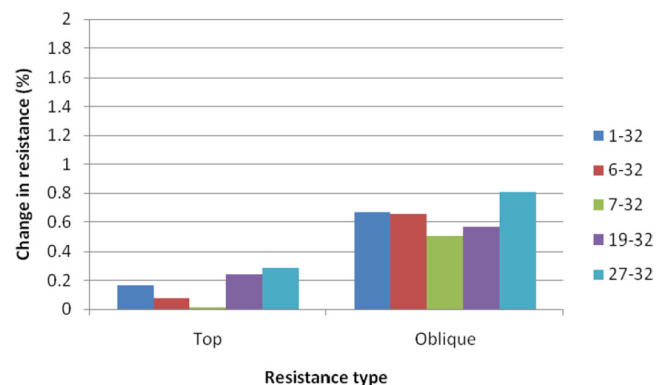


Figure 13. Percent change in resistance for the 32-ply specimens impacted at 23.02 J.

face resistance, specimen 7-32 experienced a change too insignificant to be detectable, as signified by the specimen's percent change and uncertainty. Positive percent increases in top surface resistance were detected in all of the other specimens. Specimens 1-32, 6-32, 19-32, and 27-32 exhibited percent increases of $0.17 \pm 0.05\%$, $0.08 \pm 0.05\%$, $0.23 \pm 0.08\%$, and $0.29 \pm 0.04\%$, respectively. The fact that many of the percent changes and their associated uncertainties are indistinguishable from each other correlates well with the top surface damage, since most of the damage was quite similar. As observed for the 32-ply laminates impacted at 19.91 J, the oblique resistance was more sensitive than the top surface resistance. All of the specimens experienced a change in oblique resistance that was detectable, and in each specimen the percent change in oblique resistance was greater than that for the top resistance. In fact, for a given specimen, the percent increase in the oblique resistance was anywhere from about 2.5 (specimen 19-32) to 50 (specimen 7-32) times greater than the increase in the top surface resistance. Arranged in decreasing magnitude, the percent changes in oblique resistance were as follows: $0.81 \pm 0.02\%$ (specimen 27-32), $0.67 \pm 0.04\%$ (specimen 1-32), $0.66 \pm 0.04\%$ (specimen 6-32), $57 \pm 0.05\%$ (specimen 19-32), and $0.50 \pm 0.05\%$ (specimen 7-32).

All of the 32-ply specimens impacted at 27.16 J impact energy experienced cracking within the dented region. The average dent diameter was 8.71 mm, which is about 83 percent greater than the average from the intermediate energy impacts. Like the top surfaces, the bottom surfaces of the specimens impacted at the highest energy exhibited the most damage of any impact energy. The average bottom surface damage measurements (length, width, height, delaminations) for the highest (27.16 J) impact energy were significantly larger (at least 83%) than their intermediate (23.02 J) energy counterparts.

After the impact of three 32-ply specimens at 27.16 J, the initial resistance values experienced the percent changes shown in Figure 14. Specimen 5-32 experienced a change in top surface resistance too insignificant to be detectable. With

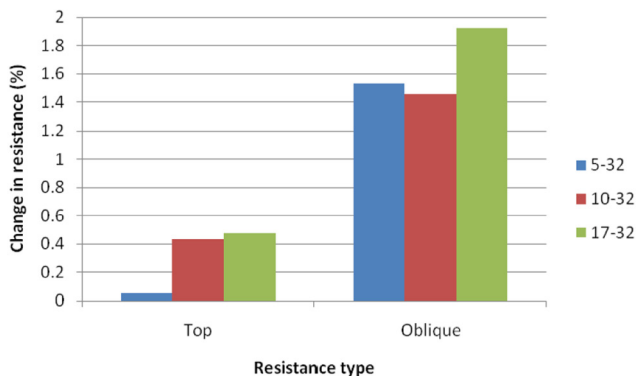


Figure 14. Percent change in resistance for the 32-ply specimens impacted at 27.16 J.

respect to sensitivity, this is an unacceptable result. Specimen 5-32, like the other two specimens at the highest impact energy, experienced a large and deep dent that should have been easily detected. This result reinforces the notion that sending current perpendicular to the surface fibers is ineffective at sensing top surface damage. Fortunately detectable increases in top surface resistance were detected in the other two specimens. Specimens 10-32 and 17-32 experienced percent increases in top surface resistance of $0.43 \pm 0.05\%$ and $0.50 \pm 0.06\%$, respectively. As observed for the lowest two impact energies, the oblique resistance was more sensitive to the highest impact energy than the top surface resistance. Specimens 5-32, 10-32, and 17-32 experienced percent changes in oblique resistance of $1.53 \pm 0.04\%$, $1.46 \pm 0.02\%$, and $1.93 \pm 0.04\%$, respectively. In other words, all of the specimens experienced a change in oblique resistance that was detectable, and in each specimen the percent change in oblique resistance was much greater than that for the top resistance. For a given specimen, the percent increase in the oblique resistance was anywhere from about 3.4 (specimen 10-32) to 25.5 (specimen 5-32) times greater than the increase in the top surface resistance. A summary of the percent changes in resistance obtained for the 32-ply specimens is provided in Table 1. As seen in the table, the lowest and intermediate impact energies produced percent changes in the top surface resistance that overlapped. While the detectable percent changes in top resistance at the highest impact energy were greater than those at the intermediate energy, both energies produced one specimen with a non-detectable change. Thus the top surface resistance was unable to distinguish between the damage states for any of the three impact energies. Similar results were found for the oblique resistance. Between the lowest and intermediate impact energies, many of the percent changes in the oblique resistance overlapped. In addition, one of the specimens impacted at the lowest energy experienced a percent change in oblique resistance of 1.79%, a change much greater than those recorded

Table 1. Percent Changes in Resistance for the 32-Ply Specimens.

Resistance Type	Impact Energy (J)		
	19.91	23.02	27.16
Top surface	0.33 ± 0.08	0.17 ± 0.05	0.43 ± 0.05
	0.10 ± 0.07	0.08 ± 0.05	0.50 ± 0.06
	0.20 ± 0.04	0.23 ± 0.08	Non-detectable
	Non-detectable	0.29 ± 0.04	Non-detectable
Oblique	0.62 ± 0.06	0.67 ± 0.04	1.53 ± 0.04
	1.79 ± 0.03	0.66 ± 0.04	1.46 ± 0.02
	0.40 ± 0.05	0.50 ± 0.05	1.93 ± 0.04
	0.75 ± 0.02	0.57 ± 0.05	
	0.78 ± 0.04	0.81 ± 0.02	

Table 2. Comparison of 32-Ply Specimens with Similar Initial Top Surface Resistances.

Specimen	Impact Energy (J)	Top Surface Resistance		Absorbed Energy (J)
		Before Impact (mΩ)	Change (%)	
20-32	19.91	7.021 ± 0.004	0.01 ± 0.08	7.13
19-32	23.02	6.984 ± 0.003	0.23 ± 0.08	6.61
5-32	27.16	7.263 ± 0.003	0.06 ± 0.06	19.82
22-32	19.91	10.045 ± 0.003	0.20 ± 0.04	7.10
27-32	23.02	11.187 ± 0.003	0.29 ± 0.04	7.22
10-32	27.16	11.161 ± 0.004	0.43 ± 0.05	20.51

for the intermediate energy. In fact, this change was larger than two of the three recorded for the highest energy. Thus the oblique resistance was also unable to distinguish between the damage resulting from the three impact energies.

As mentioned earlier for the 16-ply specimens, a significant amount of variation was present in the initial resistance values for the 32-ply specimens. To determine if this was the root cause of the percent changes not increasing with impact energy, specimens with similar initial resistances were compared. Table 2 compares specimens with similar initial top surface resistances and Table 3 compares those with similar initial oblique resistances. The first three rows of Table 2 display the results from three specimens (each representing one of the three impact energies) with initial resistances of approximately seven milliohms. The specimen impacted at the lowest energy experienced a non-detectable change in resistance, while the specimen at the intermediate energy produced a detectable increase. Unfortunately, the specimen impacted at the highest energy experienced a non-detectable change in resistance too. Therefore for the range of impact energies tested, for specimens with initial resistances of about seven milliohms, measuring the top surface resistance was not an effective damage sensing method. An effective damage sensor would not only be able to detect the damage resulting from the three impact energies, but also distinguish between the different damage states. To determine if there was a correlation

between the absorbed energy and the percent change in resistance, this data is also included in Table 2. For damage below perforation, ideally the absorbed energy should increase with increasing impact energy. In addition, the absorbed energy should ideally increase with increasing percent change in resistance. However, neither of these trends is visible in the first three rows of Table 2. The absorbed energy was smallest for the specimen impacted at the intermediate energy, the same specimen that had the greatest percent change in resistance. Fortunately, all expected trends were evident in the top surface results for the group of specimens with initial resistances of approximately 10 or 11 mΩ (bottom three rows of Table 2). Not only were all the percent changes in resistance detectable, but they also increased with increasing impact energy. The absorbed energy likewise increased with increasing impact energy. Hence the top surface resistance was an effective damage sensor for plates with initial resistances of approximately 10 or 11 mΩ.

While the top surface resistance had mixed results when comparing specimens with similar initial top surface resistances, the oblique resistance fared slightly better when a similar comparison was made for this resistance type. This comparison is shown in Table 3. The first three rows of this table show the results for specimens with an initial oblique resistance of about 12-14 mΩ. Each of these specimens had detectable increases in resistance, unlike two of those in the top surface resistance table (Table 2). However, the percent increase for the specimen impacted at the lowest energy (23-32) was larger than that for the specimen impacted at the intermediate energy (7-32), a non-ideal result. The absorbed energy data was not able to explain this result, as specimen 7-32 absorbed more energy than specimen 23-32. Fortunately the second group of specimens, with similar initial oblique resistances of about 25-26 mΩ, displayed all the expected trends in their data. Both the percent change in oblique resistance and the absorbed energy increased with increasing impact energy. This result, in conjunction with the results of the top surface comparisons, suggests that the two resistance types perform better as damage sensors when used on specimens with greater initial resistances.

Table 3. Comparison of 32-Ply Specimens with Similar Initial Oblique Resistances.

Specimen	Impact Energy (J)	Oblique Resistance		Absorbed Energy (J)
		Before Impact (mΩ)	Change (%)	
23-32	19.91	13.867 ± 0.004	0.78 ± 0.04	6.9253
7-32	23.02	12.074 ± 0.004	0.50 ± 0.05	7.9354
17-32	27.16	13.284 ± 0.004	1.93 ± 0.04	17.5956
22-32	19.91	25.097 ± 0.004	0.75 ± 0.02	7.0982
27-32	23.02	26.220 ± 0.004	0.81 ± 0.02	7.2215
10-32	27.16	25.544 ± 0.004	1.46 ± 0.02	20.5103

3.3. Cumulative Damage Studies of the 16-Ply Laminates

Three specimens (6-16, 7-16, and 15-16) were selected from the 7.19 J single impact lot to undergo cumulative damage testing. Each specimen was impacted at approximately 7.19 J until it was near perforation, which resulted in each specimen being impacted five times. Due to the damage increasing with each successive impact, it was expected that the percent changes in the initial resistances would likewise increase for each impact. For the most part, that was indeed the case. The specimen that best exhibited this behavior was specimen 15-16, whose change in resistance results are plot-

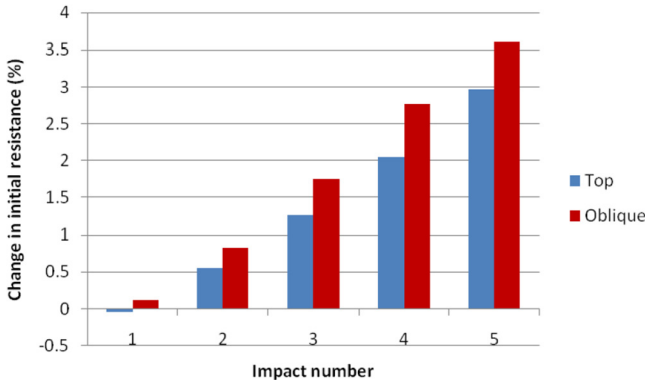


Figure 15. Percent change in resistance for specimen 15-16 during five impacts at 7.19 J.

ted in Figure 15. Several observations can be drawn from these results. First, for each successive impact and for both resistance types, the percent change in resistance increased in magnitude. Second, the change in oblique resistance was positive and detectable for every impact, while the change in the top surface resistance was non-detectable for the first impact ($-0.04 \pm 0.04\%$). Finally, the change in oblique resistance was discernibly greater than that for the top surface resistance at every impact. For these reasons, the oblique resistance was a more effective damage sensor than the top surface resistance for specimen 15-16.

Displaying slightly less ideal results than those for specimen 15-16 was specimen 7-16. As shown in Figure 16, the magnitude of the percent change in top surface resistance decreased between impacts 3 and 4 before increasing after impact five. Ideally the resistance would only increase with multiple impacts. In contrast to the top surface resistance, the magnitude of the percent change in oblique resistance either increased or remained constant with each subsequent impact. The preceding comparison is one of two reasons why the oblique resistance was a more effective damage sensor than the top surface resistance for specimen 7-16. For the second reason, the oblique resistance detected a change

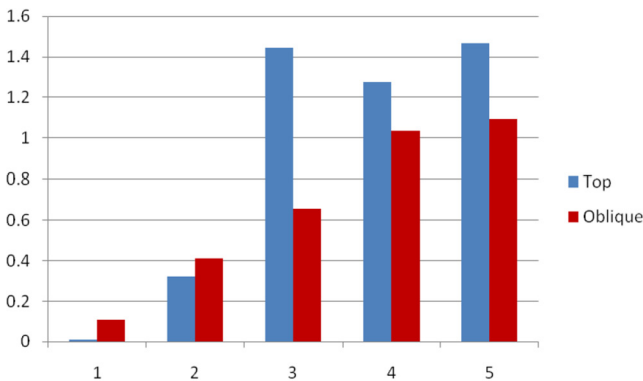


Figure 16. Percent change in resistance for specimen 7-16 during five impacts at 7.19 J.

in resistance after the first impact, while the top surface resistance did not.

Of the three specimens, the results displayed by specimen 6-16 were the least ideal. This was primarily due to the percent change in the oblique resistance being discernibly negative after the second impact, as shown in Figure 17. This negative percent change may have been caused by one or both of the following reasons. First, the leads were removed and then reattached after each impact so that the specimen could be removed from the fixture plates and inspected. While it was shown that the resistance of a specimen depended very little on the placement of the leads, there was still a slight effect. Second, the oblique resistance could have decreased due to fibers in adjacent plies coming into contact after impact. Several other observations are worth noting in the results of Figure 17.

First, the top surface resistance never experienced a decrease in initial resistance, unlike the oblique resistance. Second, the percent change in the top resistance never discernibly decreased in magnitude from impact to impact. Due to the decrease in initial resistance after the second impact, the oblique resistance automatically failed this criterion. Finally at each impact number, the percent change in the initial resistance for the top surface was either greater or indistinguishable from that for the oblique resistance. For these reasons, the top surface resistance was a more effective damage sensor than the oblique resistance for specimen 6-16.

Since the 8.67 J single impact lot consisted of only three specimens (2-16, 5-16, 11-16), all three also underwent cumulative damage testing. To obtain near-perforation damage in the specimens, three impacts at approximately 8.67 J were performed. Corresponding to the damage increasing with each successive impact, the top and oblique resistances likewise increased with each impact for all specimens. This ideal result did not always occur during the lowest energy cumulative damage study, in which two of the specimens had changes in resistance that either did not change or decreased between successive impacts. In another difference

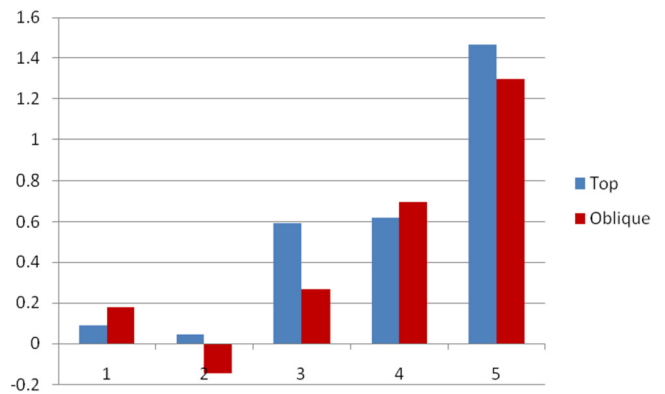


Figure 17. Percent change in resistance for specimen 6-16 during five impacts at 7.19 J.

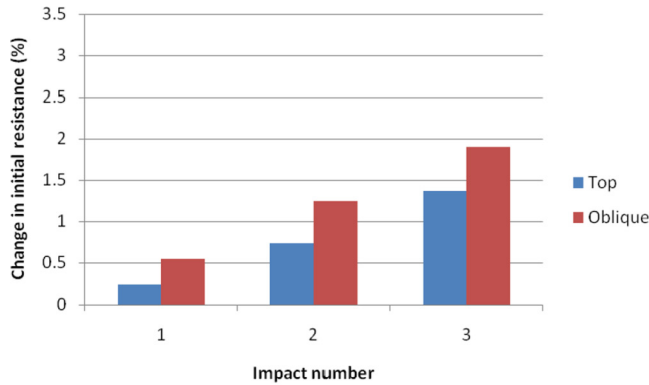


Figure 18. Percent change in resistance for specimen 2-16 during three impacts at 8.67 J.

between the two cumulative damage studies, all of the first impacts at the intermediate energy resulted in detectable increases in resistance. Both results can be attributed to the greater impact energy employed for the intermediate energy cumulative damage study. With respect to the individual specimens, both 2-16 (Figure 18) and 11-16 (omitted) experienced greater percent changes in the oblique resistance than the top surface resistance at each impact. The results of specimens 216 and 11-16 suggest that the oblique resistance was more sensitive at sensing damage than the top surface resistance for these specimens. Specimen 5-16 (Figure 19) showed the opposite result of specimens 2-16 and 11-16 with respect to sensitivity. After the first impact, the changes in top and oblique resistance were indistinguishable from each other. However, after the second and third impacts the change in the top surface resistance was greater than that for the oblique resistance. These results suggest that the top surface resistance was more effective at sensing damage than the oblique resistance for specimen 5-16. Though specimen 5-16 displayed the opposite result of specimens 2-16 and 11-16 with respect to the most sensitive resistance type, the damage observations made for specimen 5-16 do not suggest it experienced significantly different damage than the other two specimens.

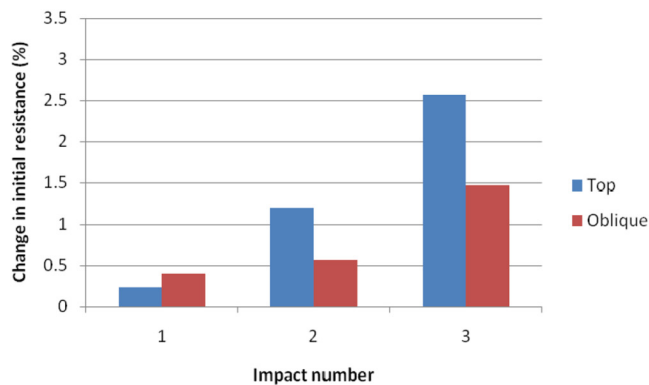


Figure 19. Percent change in resistance for specimen 5-16 during three impacts at 8.67 J.

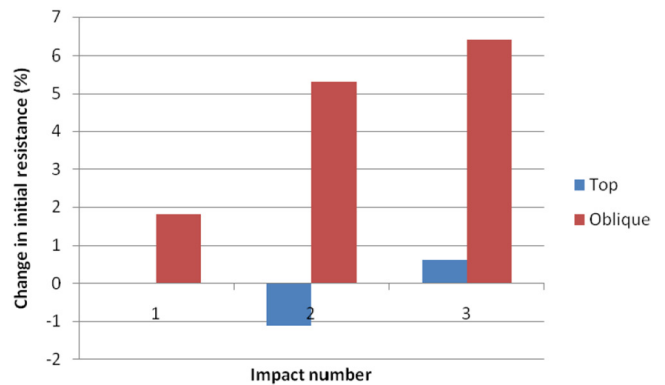


Figure 20. Percent change in resistance for specimen 20-32 during three impacts at 19.91 J.

3.4. Cumulative Damage Studies of the 32-ply Laminates After Repeated Impacts

Specimens 20-32, 21-32, and 23-32 were selected from the lowest energy, single impact specimen lot to undergo cumulative damage testing at the same energy. These specimens were subjected to three impacts at approximately 19.91 J. Overall the oblique resistance responded well to the damage caused by the impacts. The percent increases in the initial oblique resistance: were detectable after the first impact in all specimens, were significantly larger than those for the top surface resistance, and increased in magnitude with each successive impact. These trends are visible in the change in resistance plots for specimens 20-32 and 21-32 of Figures 20 and 21, respectively (the results from specimen 23-32 are omitted as they were similar to those of specimen 21-32). In general, the percent change in oblique resistance was able to differentiate between the severities of damage sustained by the specimens. For example, specimen 21-32, which experienced the least damage throughout the cumulative damage study, experienced the smallest changes in oblique resistance at each impact. On the opposite end of the spectrum, specimen 20-32 experienced the largest changes in initial oblique resistance at each impact. From the dam-

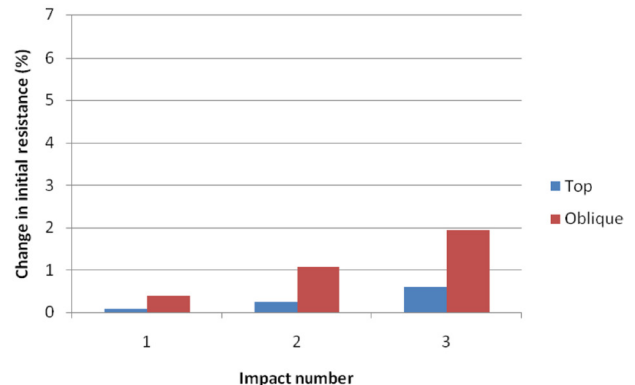


Figure 21. Percent change in resistance for specimen 21-32 during five impacts at 19.91 J.

age analyses, specimen 20-32 did indeed sustain the greatest bottom surface damage for impacts two and three, although only the second most for the first impact.

Unfortunately the top surface resistance did not perform as well as the oblique resistance in terms of sensing damage. The top surface resistance failed to detect the damage resulting from the first impact of specimens 20-32 (Figure 17) and 23-32. While the top surface resistance detected the first impact for specimen 21-32, the change in initial resistance after the second impact was not distinguishably larger than that after the first impact (Figure 18). In addition, Figure 17 shows that the top surface resistance decreased from its initial value after the second impact of specimen 20-32.

For the cumulative damage testing conducted at 23.02 J, specimens 1-32, 6-32, and 7-32 were selected from the corresponding single-impact specimen lot. These specimens were subjected to two impacts of approximately 23.02 J. As in the lowest energy cumulative damage study for the 32ply specimens, the oblique resistance proved to be an effective damage detector for the intermediate energy cumulative damage study. This observation can be noted from the change in resistance results for specimens 6-32 and 7-32 of Figures 22 and 23, respectively (the results from specimen 1-32 are omitted as they were similar to those of specimen 6-32). The oblique resistance detected the first impact in all specimens and increased significantly between the first and second impacts. The change in oblique resistance was also greater than that for the top surface resistance after both impacts of all specimens (it was significantly greater in all impacts other than impact two of specimen 7-32). While the top surface resistance did not perform as well as the oblique resistance, the top surface resistance did perform better than it did during the lowest energy cumulative damage study. For example, in the current study the top surface resistance only failed to detect the first impact in one of the specimens (Figure 20), whereas during the lowest energy cumulative damage study it produced this failure twice. In addition, the top surface resistance did not detect a decrease in resistance in the current study, unlike during the lowest energy cumu-

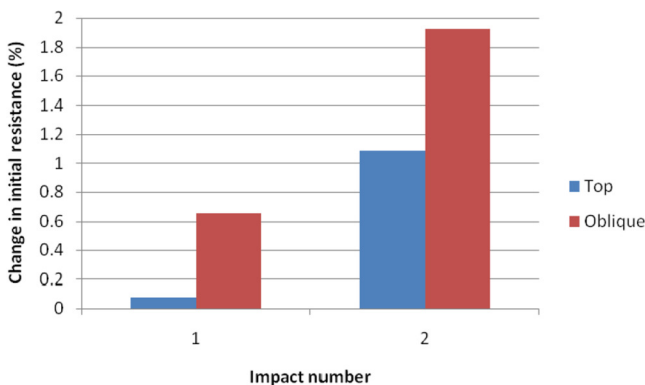


Figure 22. Percent change in resistance for specimen 6-32 during two impacts at 23.02 J.

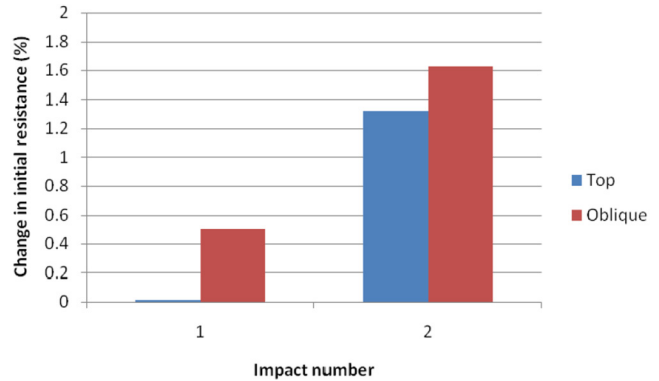


Figure 23. Percent change in resistance for specimen 7-32 during two impacts at 23.02 J.

lative damage study. Finally, the top surface resistance increased between impacts one and two for all specimens of the intermediate energy cumulative damage study, a characteristic it failed to do for two of the specimens of the lowest energy study.

4. CONCLUSIONS

The effectiveness of the one-dimensional electrical resistance method at sensing impact damage in laminate plate specimens was studied. Two types of laminates were tested: a 16-ply orthotropic $[0/45/-45/90]_{2s}$ laminate (thickness = 2.25 mm) and a 32-ply orthotropic $[0/45/-45/90]_{4s}$ laminate (thickness = 4.5 mm). Four contacts were placed on both the top and bottom surfaces of the specimens such that they extended across the entire surface. These contacts were placed parallel to the surface fiber direction, as preliminary testing with perpendicular contacts proved ineffective (at low impact energies, the changes in resistance could not be detected, while at higher impact energies the bottom surface damage caused the electrodes to come off the surface). Single impact and cumulative damage studies were conducted for both the 16- and 32-ply specimens. Before and after each impact, the top surface resistance and the oblique resistance (resistance through the thickness of the specimen at an oblique angle) of the impact region were measured.

In general, the oblique resistance proved to be more sensitive to impact damage than the top surface resistance for the single impact studies. The top surface resistance failed to detect the impact damage in several of the specimens, including some that were impacted at large energies and displayed significant top surface damage. Overall however, neither resistance type proved to be effective at sensing damage in plate specimens. For the 16-ply specimens, both produced negative percent changes in resistance for one specimen at the lowest impact energy. In addition, both resistance types produced changes in resistance that overlapped for the intermediate and highest impact energies. Thus the resistance types were unable to distinguish between the severities of

damage caused by these two impact energies. For the 32-ply specimens, the top surface resistance and the oblique resistance were unable to distinguish between the damage at any of the three impact energies. This lack of a direct relationship between the impact energy and the change in resistance was partly due to the large variation in initial resistances recorded for the specimens. However, even when specimens with similar initial resistances were compared, the changes in resistance did not always increase with increasing impact energy.

Overall the resistance types displayed better results during the cumulative damage studies than during the single impact tests. During the cumulative damage tests at the intermediate energies for both the 16- and 32-ply specimens, both the top surface resistance and the oblique resistance increased with each successive impact. During the tests at the lowest energies, however, this was not always the case. Some of the specimens exhibited percent increases in resistance that either stayed constant or decreased between impacts. Each of the lowest energies also produced a specimen that displayed a decrease in initial resistance, one for the oblique resistance, the other for the top surface resistance.

Based on the findings from both the single impact and cumulative damage studies, the resistance method has had a limited success at sensing impact damage in AS4/3501-6 laminate composite plate specimens due to very low initial resistances of the composites tested.

5. REFERENCES

- [1] Schulte, K. and Baron, C., "Load and Failure Analysis of CFRP Laminates by Means of Electrical Resistivity Measurements", *Composites Science and Technology*, Vol. 36, 1989, pp. 63–76. [http://dx.doi.org/10.1016/0266-3538\(89\)90016-X](http://dx.doi.org/10.1016/0266-3538(89)90016-X)
- [2] Prasse, T., Michel, F., Mook, G., Schulte, K., and Bauhofer, W., "A Comparative Investigation of Electrical Resistance and Acoustic Emission During Cyclic Loading of CFRP Laminates", *Composites Science and Technology*, Vol. 61, 2001, pp. 831–835. [http://dx.doi.org/10.1016/S0266-3538\(00\)00179-2](http://dx.doi.org/10.1016/S0266-3538(00)00179-2)
- [3] Angelidis, N., Khemiri, N., and Irving, P. E. "Experimental and Finite Element Study of the Electrical Potential Technique for Damage Detection in CFRP Laminates", *Smart Materials and Structures*, Vol 14, 2005, pp.147–154. <http://dx.doi.org/10.1088/0964-1726/14/1/014>
- [4] Wang, D., Wang, S., Chung, D. D. L., and Chung, J. H. 2006. "Comparison of the Electrical Resistance and Potential Techniques for the Self-sensing of Damage in Carbon Fiber Polymer-Matrix Composites," *J. Intell. Mats. Sys. & Struct.*, 17(10):853–861. <http://dx.doi.org/10.1177/1045389X06060218>
- [5] Chung, D. D. L. 2007. "Damage detection using self-sensing concepts," *Proceedings of the Institution of Mechanical Engineers Part G-Journal of Aerospace Engineering*, 221(G4):509–520. <http://dx.doi.org/10.1243/09544100JAERO203>
- [6] Wang, S., and Chung, D. D. L. 2005. "Effects of composite lay-up and thickness on the damage self-sensing behavior of carbon fiber polymer-matrix composite," *Journal of Materials Science*, 40(3):561–568. <http://dx.doi.org/10.1007/s10853-005-6289-6>
- [7] Wang, S. K., Chung, D. D. L., and Chung, J. H. 2005. "Impact damage of carbon fiber polymer-matrix composites, studied by electrical resistance measurement," *Composites Part A-Applied Science and Manufacturing*, 36(12):1707–1715. <http://dx.doi.org/10.1016/j.compositesa.2005.03.005>
- [8] Wang, S. K., Chung, D. D. L., and Chung, J. H. 2005. "Self-sensing of damage in carbon fiber polymer-matrix composite by measurement of the electrical resistance or potential away from the damaged region," *Journal of Materials Science*, 40(24):6463–6472. <http://dx.doi.org/10.1007/s10853-005-1708-2>
- [9] Wang, D., Wang, S., Chung, D. D. L., and Chung, J. H. 2006. "Sensitivity of the two-dimensional electric potential/resistance method for damage monitoring in carbon fiber polymer-matrix composite," *Journal of Materials Science*, 41(15):4839–4846. <http://dx.doi.org/10.1007/s10853-006-0062-3>
- [10] Shen, L., Li, J., Liaw, B. M., Delale, F., and Chung, J. H. 2007. "Modeling and analysis of the electrical resistance measurement of carbon fiber polymer-matrix composites," *Composites Science and Technology*, 67(11-12):2513–2520. <http://dx.doi.org/10.1016/j.compscitech.2006.12.020>
- [11] Todoroki, A., Omagari K., Shimamura, Y., Kobayashi H. 2006. "Matrix crack detection of CFRP using electrical resistance change," *Composites Science and Technology*, 66:1539–1545. <http://dx.doi.org/10.1016/j.compscitech.2005.11.029>
- [12] Hirano, Y., Todoroki, A. 2007. "Damage identification of woven graphite/epoxy composite beams using the electrical resistance change method," *Journal of Intelligent Material Systems and Structures*, 18:253–263. <http://dx.doi.org/10.1177/1045389X06065467>
- [13] Todoroki, A. 2008. "Delamination Monitoring Analysis of CFRP Structures using Multi-Probe Electrical Method," *Journal of Intelligent Material Systems and Structures*, 19:291–298. <http://dx.doi.org/10.1177/1045389X07084154>
- [14] ACEE Composites Project Office (1982). *Standard tests for toughened resin composites* (NASA RP-1092). Hampton, Virginia: NASA-Langley.



Effect of Process Parameters on the Dynamic Modulus, Damping and Energy Absorption of Vertically Aligned Carbon Nano-Tube (VACNT) Forest Structures

P. RAJU MANTENA^{1,*}, BRAHMANANDA PRAMANIK¹, TEZESWI TADEPALLI¹, VEERA M. BODDU², MATTHEW W. BRENNER² and ASHOK KUMAR²

¹Composite Structures and Nano-Engineering Research, Department of Mechanical Engineering, University of Mississippi, University, MS 38677, USA

²U. S. Army Engineer Research and Development Center - Construction Engineering Research Laboratory (ERDC-CERL), Champaign, IL 61821, USA

KEYWORDS

VACNT
silicon substrate
Dynamic Mechanical Analysis
Split-Hopkinson Pressure Bar

ABSTRACT

Functionally graded materials (FGMs) are a new generation of engineered materials wherein the micro-structural details are spatially varied through non-uniform distribution of the reinforcement phase(s). The dynamic mechanical behavior and high-strain rate response characteristics of a functionally graded material system consisting of vertically aligned carbon nanotube ensembles grown on silicon wafer substrate (VACNT-Si) and processed at various temperatures have been characterized. Flexural rigidity (storage modulus) and the loss factor (damping) were measured with a dynamic mechanical analyzer in an oscillatory three-point bending mode. It was found that the functionally graded VACNT-Si processed at 770°C and 820°C exhibited higher damping without sacrificing flexural rigidity. A Split-Hopkinson Pressure Bar (SHPB) was used for determining the dynamic response under high-strain rate compressive loading. It was again observed that the VACNT-Si specimens processed at 770°C and 820°C showed a large increase in specific energy absorption, compared with those processed at 720°C. Interfacial friction between individual VACNTs, caused by their alignment/entanglements under cyclic deformation, is believed to be the primary energy dissipation mechanism for such large improvement in loss factor (compared to base Silicon wafer substrate). The larger height of VACNT forest depositions for specimens processed at 770°C and 820°C may have caused more entanglements, as reflected in higher damping and specific energy absorption. It appears that the optimal processing temperature may be around 770°C for attaining the highest damping and specific energy absorption, in terms of height and alignment/entanglement of the VACNTs grown on Si-wafer substrate.

© 2014 DEStech Publications, Inc. All rights reserved.

1. INTRODUCTION

Various biological structures rely on an architecture similar to foam core sandwich structures that are strong, resilient, light weight, and robust. Nanoparticle enhanced structures can exhibit both improved functionality and simplified assembly using graded materials. Increasing the energy dissipation characteristics of carbon nanotubes (CNTs), by

introducing stiffness gradients through topological defects and entanglements, is a novel concept which will be helpful for designing light-weight blast and impact resistant protection systems. The controlled experimental characterization of such hierarchical composite structures under high-strain shock and impact loading would provide valuable insights for designing structures to mitigate the effects of natural and man-made disasters. Such a characterization of CNT based materials has been carried out at high strain rates on resin based composites [1,2], but this has not yet been reported for a pure CNT forest on a silicon substrate.

*Corresponding author. E-mail: mepm@olemiss.edu; Tel: (662) 915-5990; Fax: (662) 915-1640

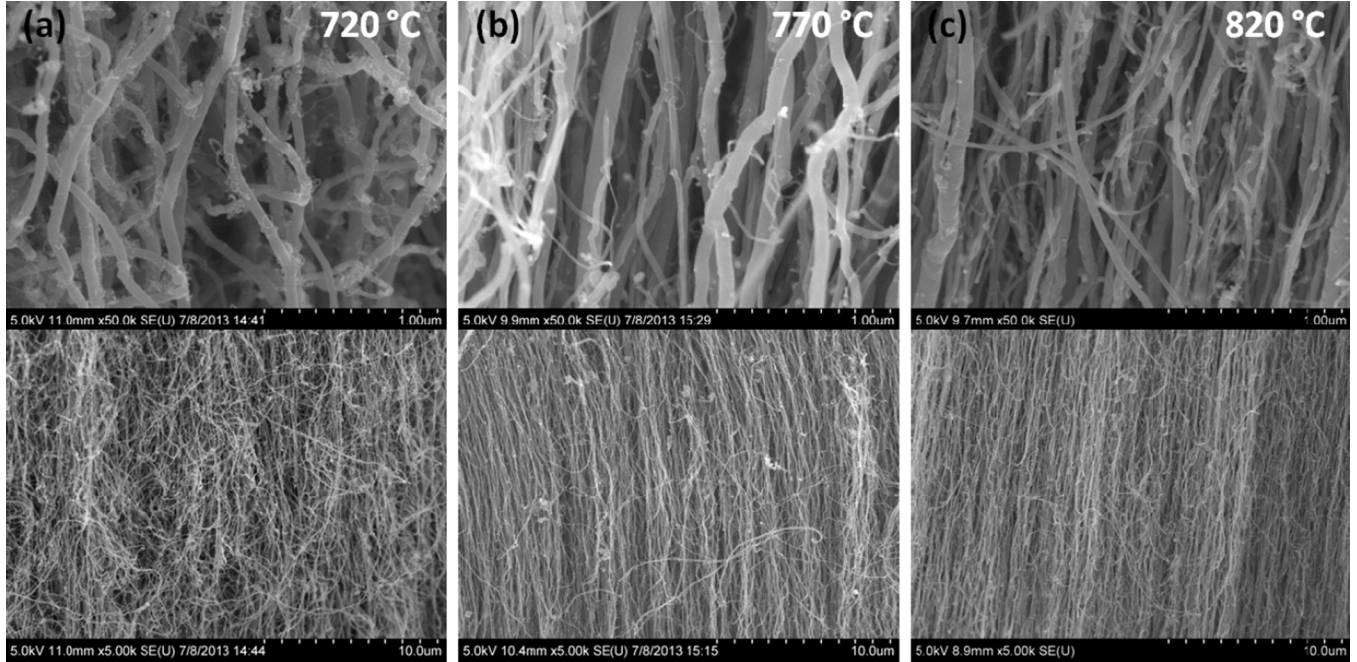


Figure 1. Multiwall VACNT forests synthesized using the chemical vapor deposition approach grown at (a) 720°C, (b) 770°C, and (c) 820°C (shown at two different magnifications).

In the work reported here, straight vertically aligned carbon nanotube (VACNT) forests are grown on silicon wafer substrates using the well established chemical vapor deposition (CVD) approach [3,4]; the details of which are described in an earlier paper by the authors [5]. The VACNT forests used in this study are grown using m-xylene as a source of carbon and ferrocene as the catalyst at various temperatures; including 720, 770 and 820°C. Figure 1 shows scanning electron micrographs of the VACNT forests grown at these three temperatures, at two different magnifications. It can clearly be observed that the vertical alignment increases with process temperature. However, some variation in the mechanical properties of these CNTs synthesized at different temperatures may be expected due to thermal conditions these VACNTs were exposed to during the synthesis process. In the following sections, the effect of process parameters on the dynamic modulus, damping and energy absorption of such graded VACNT forest structures are presented.

2. EXPERIMENTS AND ANALYSIS

2.1. Dynamic Mechanical Analysis

The dynamic mechanical properties of pure Si wafer and VACNT-Si [Figure 2(a) and (b) inset] processed at 720°C, 770°C and 820°C were analyzed with a TA Instruments Model Q800 DMA [6,3]. The 6 mm (0.24 inches) wide, 0.4 mm (0.016 inches) thick and 55 mm (2.17 inches) long pure silicon wafer rectangular beam specimen was processed in

a similar way as the VACNT-Si specimens, except for the introduction of carbon source and ferrocene. It was observed that the height of VACNT forest ensembles (grown on one side of the silicon wafer) was about 0.25 mm for the 720°C, 0.7 mm for 770°C and 0.6 mm for the 820°C processed samples. DMA tests were conducted using three-point oscillatory bending mode for evaluating the dynamic modulus and loss factor (damping) of both pure Si wafer and the VACNT-Si specimens processed at 720°C, and 770°C and 820°C.

The specimens were simply supported on two free roller-pins 50 mm apart and loaded by a fixed roller-pin from top at mid-span of the specimen [Figure 2(a)]. The VACNTs were locally removed from the specimen-roller contact areas [Figure 2(b)], to eliminate localized crushing of VACNTs during the test. The DMA tests were conducted at 10 μm amplitude and 1 Hz oscillation frequency along with temperature ramp from ambient (30°C) to 120°C, at 2°C·min⁻¹ heating rate. The dynamic mechanical parameters, such as storage modulus (E'), loss modulus (E'') and $\tan \delta$ (damping loss factor, ratio of E'' to E') were estimated from the required amount of force (F) and corresponding sample response-delay in phase angle (δ) according to the DMA stiffness model for a rectangular cross-section specimen under three-point bending load condition as given [8] in Equations (1)–(4):

$$E = K \cdot G \quad (1)$$

$$K = \frac{F}{d} \quad (2)$$

$$G = \left(\frac{L^3}{6I} \right) \left[1 + \frac{6}{10} (1 + \nu) \left(\frac{t}{L} \right)^2 \right] \quad (3)$$

$$E' = E \cos \delta \quad (4)$$

where E = elastic modulus, K = estimated stiffness, G = geometry factor, F = measured force, d = pre-specified amplitude, L = length (half span), $I = bt^3/12$ (area moment of inertia of beam cross-section), b = beam width, t = thickness and ν = specimen Poisson's ratio.

The DMA output data are influenced by the specimen thickness and Poisson's ratio inputs. Since loading and support pins were directly in contact with Si wafer surface for both pure Si wafer and VACNT-Si specimens [Figure 2(b)], the pure Si wafer thickness of 0.4 mm (0.016 inches) was also used as the effective thickness for VACNT-Si specimens. Due to non-availability of Poisson's ratio for the VACNTs, in-plane Poisson's ratio of $\nu_{xy} = 0.064$ for ortho-

tropic pure silicon wafer [9] has been considered for both pure Si wafer and the VACNT-Si DMA test specimens.

2.2. High-Strain Rate Testing

The high-strain rate testing of pure Si wafer and VACNT-Si was conducted using a Split Hopkinson Pressure Bar (SHPB, also known as Kolsky Bar). It is capable of testing materials at high compressive strain rates typically ranging from 10^2 to 10^4 per second depending on the bar length and requirements of stress equilibrium and constant strain rate [5,10].

The energy absorbing capacity of the specimen is defined as the energy required for deforming a given specimen to a specific strain [11]. The energy absorbed per unit volume up to ultimate failure strain ϵ_u can be evaluated by integrating the area under the stress (σ_s)-strain (ϵ_s) curve for each specimen as shown in Equation (5):

$$\omega = \int_0^{\epsilon_u} \sigma_s d\epsilon_s \quad (5)$$

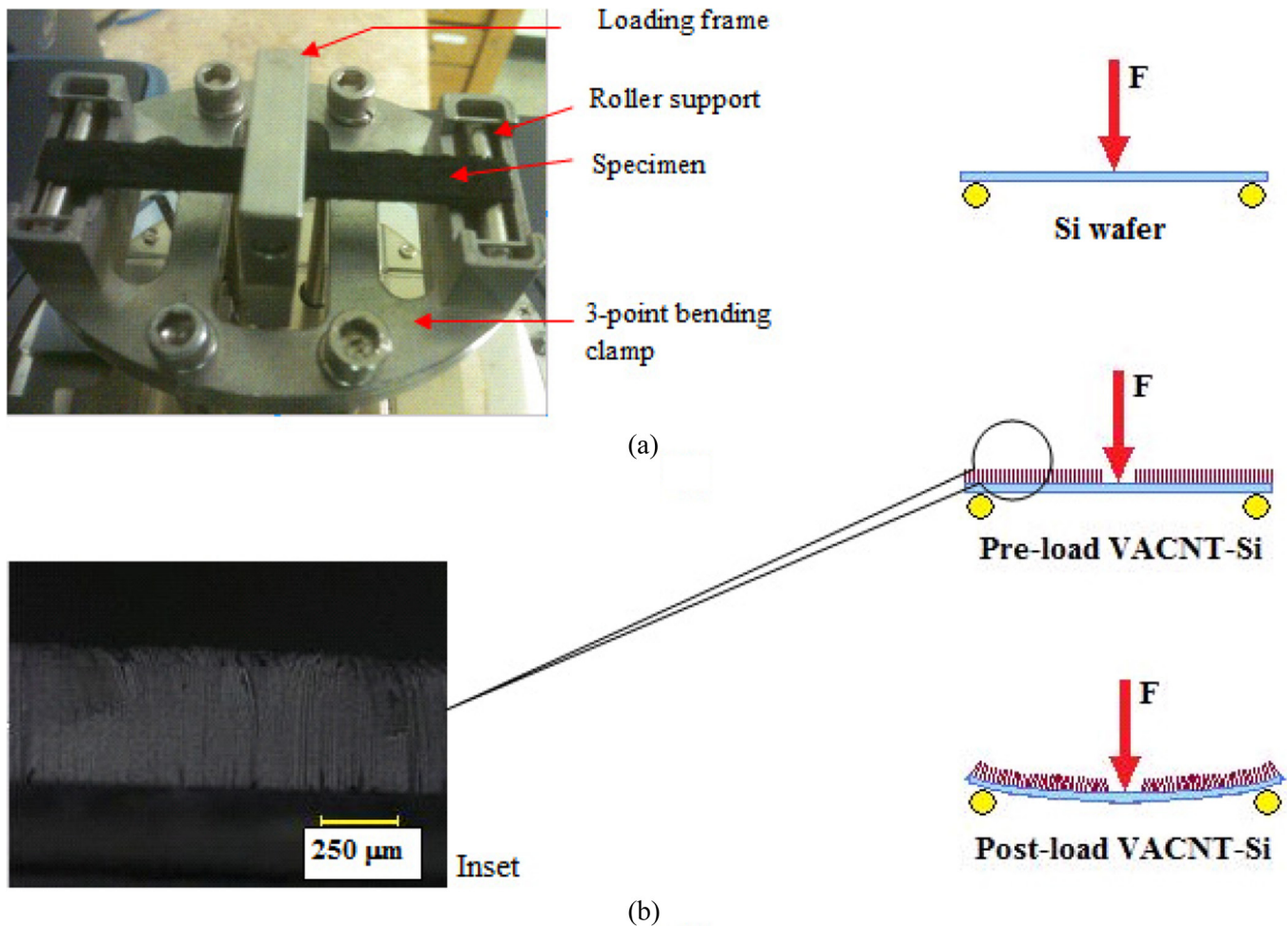


Figure 2. Experimental set-up for DMA testing; (a) sample in three-point bending at a prespecified $10 \mu\text{m}$ amplitude and 1 Hz oscillation frequency, and (b) energy dissipation caused by the entanglement of VACNTs on silicon wafer substrate during cyclic flexural deformation (Inset: digital microscope image of VACNTs on silicon wafer substrate) [5].

The diameter of the SHPB is 0.75 inches (19.05 mm), so the maximum size of a square sample that can fit is 0.5 inches (12.7 mm) on each side. In the current study layered specimens that are a combination of soft and flexible (VACNTs) and very hard (Silicon) materials are investigated. The soft VACNT forest layer requires the use of low impedance bars made of materials such as aluminum or polycarbonate. However, due to the hard silicon wafer substrate, there is an increased possibility for bars made of these softer materials to get scoured/dented, which necessitates the usage of harder maraging steel bars.

The specimens need to be dimensioned such that the thickness to side ratio (aspect ratio) is optimized for a good response signal during SHPB testing. The aspect ratio of the specimen controls the strain rate as well. The range for aspect ratios is different for soft materials and hard materials [10,12]. For soft materials, the range of thickness/diameter aspect ratio (for circular specimens) is between 0.25–0.5. In the case of metals it is between 0.5–1.0 and for ceramics it is between 1.0–2.0. There are other considerations as

well, that depend on the specimen dimensions such as stress equilibrium (thickness dependent), friction and radial inertia (diameter dependent).

The VACNT-Si specimens were placed with the Si substrate on the incident bar side and the VACNT coating facing the transmission bar side. Glycerin was applied as couplant between the Si substrate and the incident bar face. The transmission bar was carefully placed in contact with the VACNT forest layer surface without pre-compressing the forest layer. The tests were conducted at constant force (as determined by a reservoir pressure of 10 psi applied to the striker bar). Since this is a new material system, geometry trials with various specimen sizes were evaluated. Specific results for square samples of approximate size 6 mm (0.24 inches) \times 6 mm (0.24 inches) \times 0.4 mm (0.016 inches) for the pure Si-wafer and 6 mm (0.24 inches) \times 6 mm (0.24 inches) \times 1 mm (0.039 inches) for VACNT-Si are reported here. Three specimens each of pure Si wafer and VACNT-Si processed at 720°C, 770°C and 820°C were tested in compression and the results analyzed.

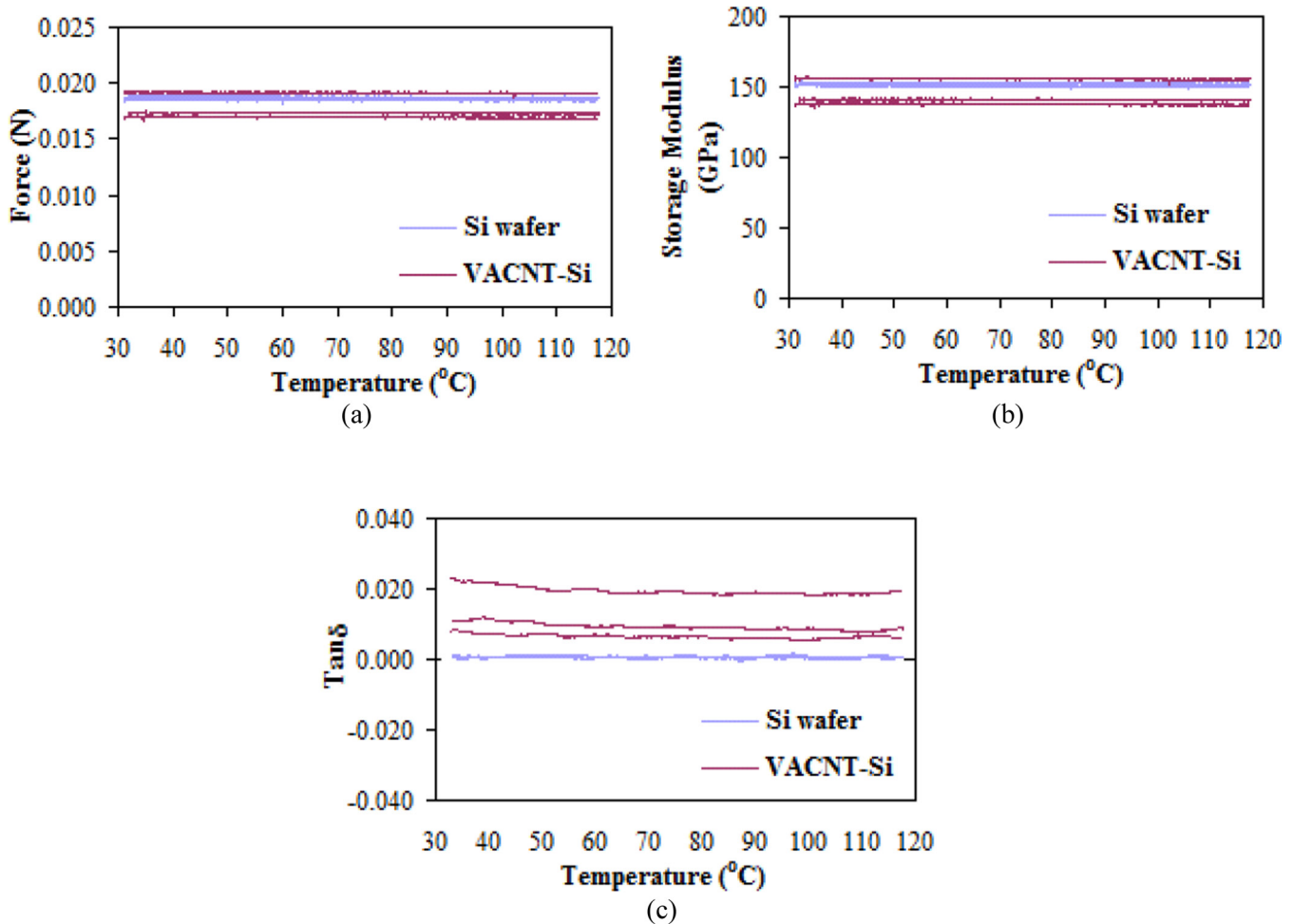


Figure 3. Typical DMA results for three specimens each of pure Si wafer and VACNT-Si (processed at 820°C) analyzed over a temperature range from ambient (30°C) to 120°C; (a) the required line force F at mid-span to achieve 10 μm amplitude; (b) the 'apparent' storage modulus, E' ; and (c) associated damping loss factor, $\text{Tan } \delta$.

3. RESULTS

Three specimens each of pure Si wafer and VACNT-Si for each processing temperatures were tested in the DMA under three-point oscillatory flexural load over a temperature range from ambient temperature (30°C) to 120°C. The flexural rigidity and damping of these specimens were investigated in terms of the required force [F , line force at mid-span to achieve 10 μm amplitude—Figure 3(a)], ‘apparent’ storage modulus [E' , Figure 3(b)], and the damping loss factor [$\tan \delta$, ratio of dissipated energy to stored energy—Figure 3(c)]. As can be observed, these values remain constant over the 120°C test temperature range; without a demonstrated peak of loss factor along with drop in storage modulus, which is more typical for viscoelastic materials around their glass transition temperature [2,7].

Both the required force and ‘apparent’ storage modulus show a negligible drop for the VACNT-Si specimens, but still within experimental scatter. This could perhaps be attributed to some degradation and/or chemical erosion of specimen surface during the growth of VACNTs at an elevated temperature. On the other hand, damping loss factor ($\tan \delta$) shows a remarkable increase for the samples with VACNTs grown on pure Si wafer [Figure 3(c)]. Interfacial friction among the densely grown VACNTs when subjected to flexural oscillations may be the contributing energy dissipation mechanism which dictates the loss factor. Specimens processed at 720°C, 770°C and 820°C show a similar trend of dynamic response (Figure 4). However, the VACNT-Si processed at 770°C and 820°C show higher damping loss factor along with a large data scatter. As noted earlier, the height of VACNTs processed at 770°C and 820°C were about 0.7 mm and 0.6 mm respectively, which is larger than that (~ 0.25 mm) of the VACNTs processed at 720°C. Also, non-uniform height of VACNTs along the length of specimens processed at 770°C could be a reason for this large data scatter.

As mentioned previously, the combination of soft VACNT forest layer with a hard silicon wafer presented novel challenges for SHPB testing. The response of VACNT forest layer is typical of an open-cell foam structure consisting of well-arranged one-dimensional units [13]. Various energy absorption mechanisms such as localized higher mode buckling of VACNTs under static compressive loading and nano-indentation along with surface entanglement and van der Waals interactions with neighboring nanotubes have been reported in literature [14,15].

Even though the tests were conducted at a constant force as mentioned earlier, due to the impedance mismatch at the interface of the Si and VACNT layers in the VACNT-Si specimens, higher amplitude reflected pulses (ϵ_r) of longer time duration are obtained, in comparison with pure Si wafer specimens. Thus the specimen strains as well as strain rates are also higher in comparison with the response of

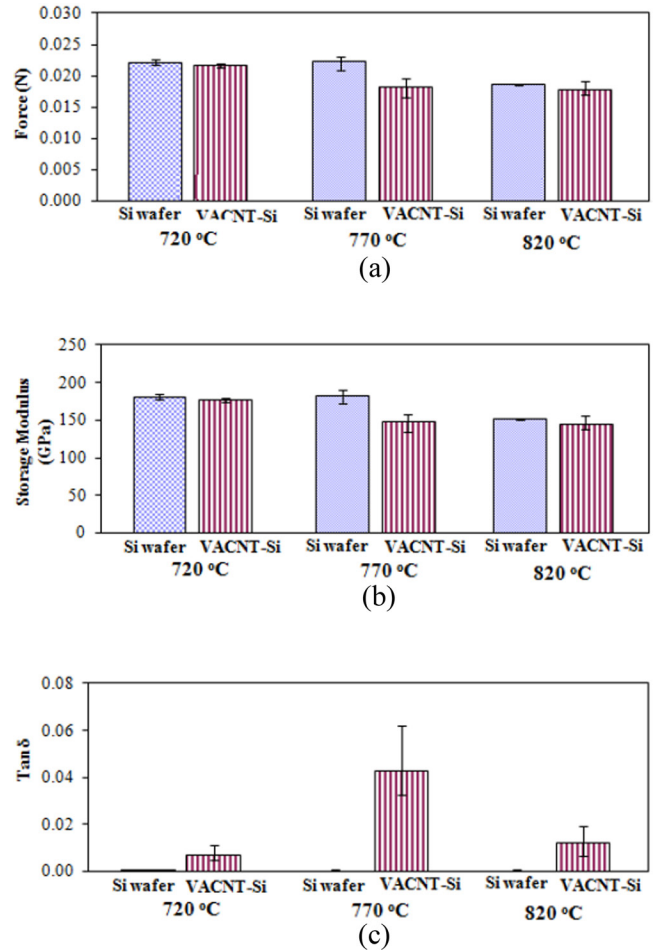


Figure 4. DMA results for three specimens each of pure Si wafer and VACNT-Si processed at 720°C, 770°C and 820°C; (a) the required line force at mid-span to achieve 10 μm amplitude; (b) the ‘apparent’ storage modulus, E' ; and (c) associated damping loss factor, $\tan \delta$.

pure Si wafer specimens. However, it is observed that the time duration of transmitted pulses (ϵ_t) reduces proportionately in order to satisfy energy conservation at the specimen-bar interface. Thus higher stresses are obtained at smaller strains in the case of VACNT-Si specimens. As a result, all the VACNT-Si specimens show larger strains to failure, as well as higher peak stress (Figures 5, 6 and 7), which translates into higher toughness and energy absorption capacity in comparison with corresponding pure Si-wafer.

Since the nano-reinforced functionally graded material systems are being developed for light weight structural applications; the specific energy absorption, given by the ratio of energy absorbing capacity [Equation (5)] and the mass density, is reported in Figures 8 and 9.

In case of specimens processed at 720°C, an average increase of around 270% was observed in specific energy absorption (kJ/kg) by VACNT-Si layered specimens in comparison with pure Si wafer (Figure 8), for the above mentioned strain rates. It was also observed that the VACNT-

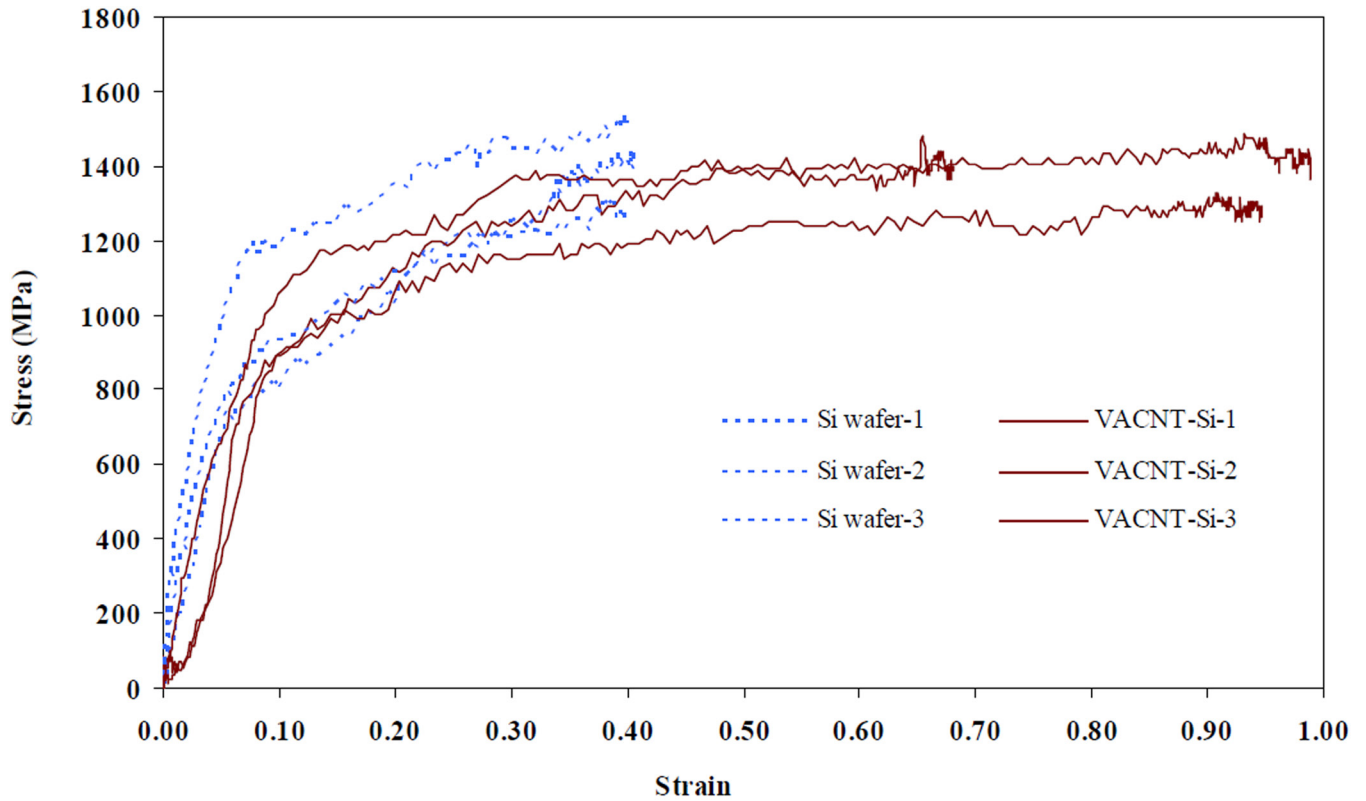


Figure 5. High strain rate response of pure Si-wafer and VACNT-Si (processed at 720°C) over the strain rate range of 6000/s to 9000/s.

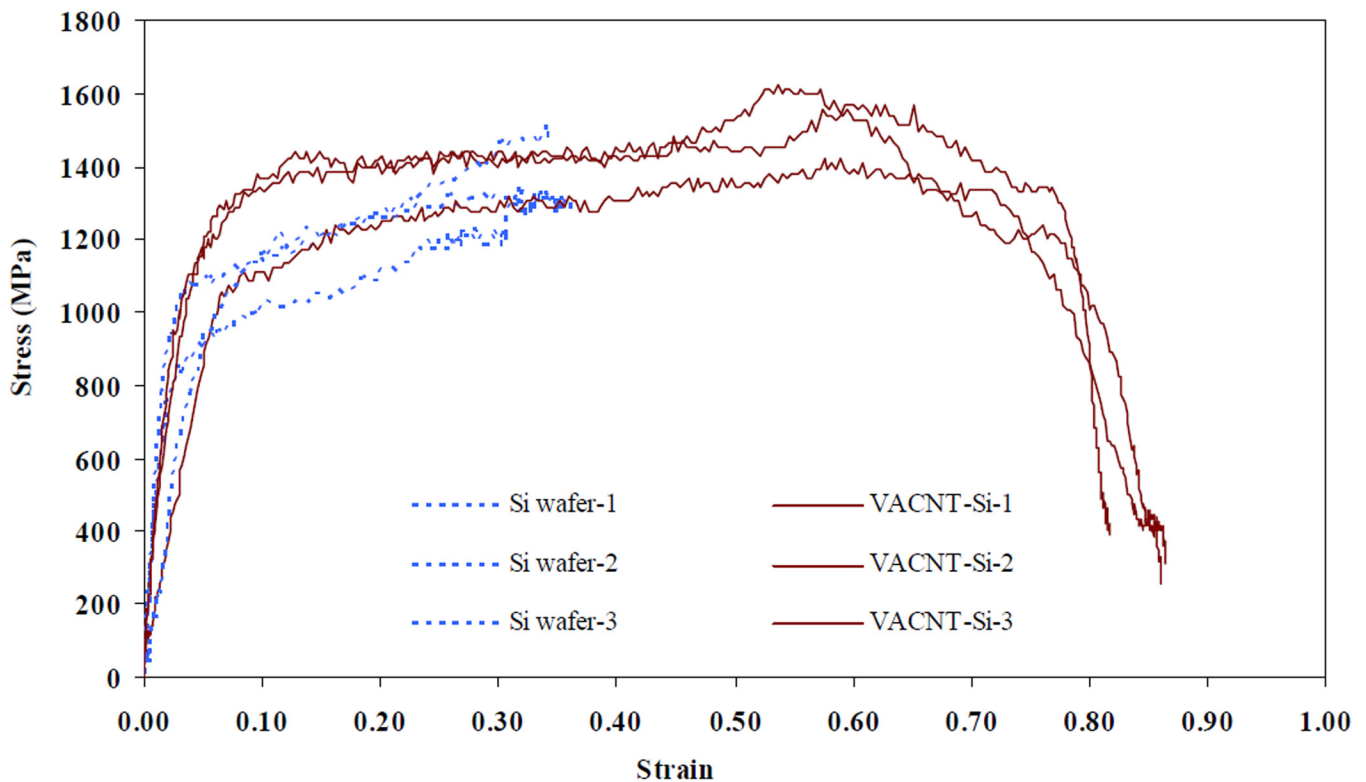


Figure 6. High strain rate response of pure Si-wafer and VACNT-Si (processed at 770°C) over the strain rate range of 3500/s to 7500/s.

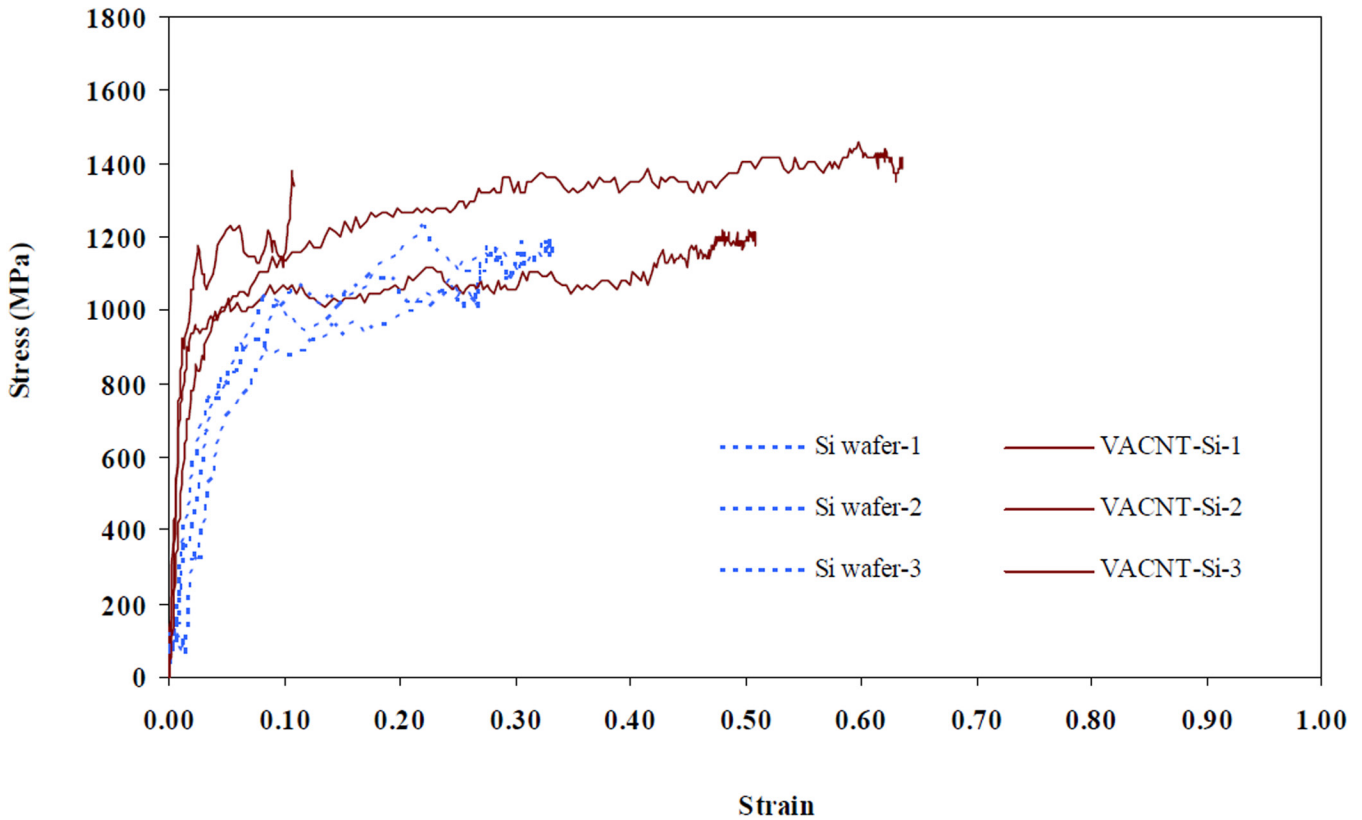


Figure 7. High strain rate response of pure Si-wafer and VACNT-Si (processed at 820°C) over the strain rate range of 6000/s to 9000/s.

Si specimens achieved an average increase of around 30% in the rate of specific energy absorption (GJ/kg-s), when compared with the corresponding pure Si wafer (Figure 9). For specimens processed at 770°C, an average increase of around 600% was observed in specific energy absorption (kJ/kg) by VACNT-Si layered specimens in comparison with pure Si wafer specimens for the strain rates mentioned above (Figure 8). It was also observed that the VACNT-Si specimens achieved an average increase of around 95% in the rate of specific energy absorption (GJ/kg-s), when compared with the corresponding pure Si wafer (Figure 9). In case of specimens processed at 820°C, an average increase of around 260% in specific energy absorption (kJ/kg) was observed for VACNT-Si layered specimens in comparison

with pure Si wafer specimens for the strain rates mentioned above (Figure 8). Also, the VACNT-Si specimens achieved an average increase of around 30% in the rate of specific energy absorption (GJ/kg-s), when compared with the corresponding pure Si wafer (Figure 9). It appears that around 770°C may be the optimal processing temperature for attaining the highest specific energy absorption, in terms of both height and alignment/entanglement of the VACNTs.

4. CONCLUSIONS

The dynamic mechanical behavior of a functionally graded material system consisting of vertically aligned carbon nanotube ensembles grown on a silicon wafer substrate

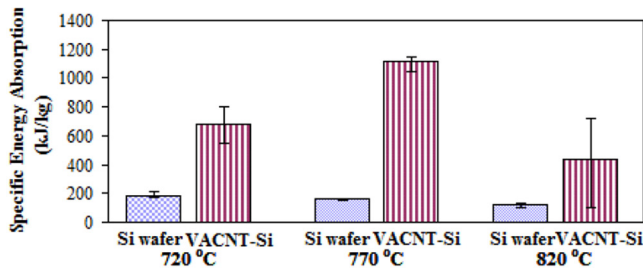


Figure 8. Specific energy absorption of pure Si-wafer and VACNT-Si (processed at 720°C, 770°C and 820°C).

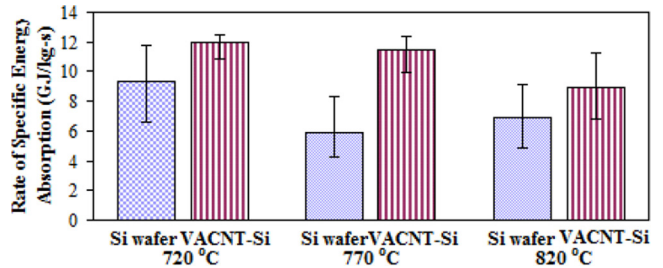


Figure 9. Rate of specific energy absorption for pure Si-wafer and VACNT-Si (processed at 720°C, 770°C and 820°C).

(VACNT-Si) processed at 720°C, 770°C and 820°C has been investigated. The functionally graded VACNT-Si exhibited significantly higher damping than that showed by the pure Si-wafer without sacrificing the flexural rigidity. Interfacial friction between individual VACNTs caused by their entanglements under cyclic deformation is believed to be the primary energy dissipation mechanism for such a large improvement in loss factor. The VACNT-Si processed at 770°C and 820°C demonstrated higher damping than the specimens processed at 720°C, without sacrificing their flexural rigidity. The larger height of VACNT ensemble deposition for the 770°C (0.7 mm) and 820°C (0.6 mm) processed specimens could have resulted in this higher damping. In the case of high-strain rate compressive loading, large increase in specific energy absorption as well as the rate of specific energy absorption was observed for the VACNT-Si layered specimens, compared with pure Si wafer.

5. ACKNOWLEDGMENT

This research was funded by Grant # W9132T-12-P0057 from the US Army Engineer Research and Development Center—Construction Engineering Research Laboratory (ERDC-CERL), Champaign, IL; and approved for public release with unlimited distribution. The authors would like to thank Mr. Damian Stoddard and Mr. Kiyun Kim, mechanical engineering graduate students at the University of Mississippi, for their help with the DMA and Hopkinson bar experiments.

6. REFERENCES

- [1] S. Pande, P. Sharma, V. Mangla, A. Chaudhury, D. Patel, B. P. Singh, R. B. Mathur, M. Goyal, "High strain rate behavior of multi-walled carbon nanotubes-polycarbonate composites," *Composites Part B: Engineering* 45(1), 417 (2013). <http://dx.doi.org/10.1016/j.compositesb.2012.06.018>
- [2] A. S. Lim, Q. An, T.-W. Chou, "Mechanical and electrical response of carbon nanotube-based fabric composites to Hopkinson bar loading," *Composites Sci. and Tech.* 71(5), 616 (2011). <http://dx.doi.org/10.1016/j.compscitech.2010.12.025>
- [3] C.M. Seah, S.P. Chai, A. R. Mohamed, "Synthesis of aligned carbon nanotubes," *Carbon* 49(14), 4613 (2011). <http://dx.doi.org/10.1016/j.carbon.2011.06.090>
- [4] E.G. Rakov, "Materials made of carbon nanotubes. The carbon nanotube forest," *Russ. Chem. Rev.* 82(6), 538 (2013). <http://dx.doi.org/10.1070/RC2013v082n06ABEH004340>
- [5] P. R. Mantena, T. Tadepalli, B. Pramanik, V. M. Boddu, M. W. Brenner, L. D. Stephenson, and A. Kumar, "Energy dissipation and the high-strain rate dynamic response of vertically aligned carbon nanotube (VACNT) ensembles grown on silicon wafer substrate," *Journal of Nanomaterials*, vol. 2013 (2013), Article ID 259458, 7 pages, doi: 10.1155/2013/259458
- [6] Y. Zeng, L. Ci, B. J. Carey, R. Vajtai, and P. M. Ajayan, "Design and reinforcement: vertically aligned carbon nanotube-based sandwich composites," *ACS Nano* 2010, vol. 4, no. 11, pp. 6798-6804. doi: 10.1021/nn101650p
- [7] B. Pramanik, and P. R. Mantena, "Viscoelastic response of graphite platelet and CTBN reinforced vinyl ester nanocomposites," *Materials Sciences and Applications*, 2011, vol. 2, no. 11, pp. 1667-1674. doi: 10.4236/msa.2011.211222
- [8] Dynamic Mechanical Analyzer, Q Series, Calculation based on clamp type, Revision F, TA Instruments, New Castle, Del, USA, 2004.
- [9] M. A. Hopcroft, W. D. Nix, and T. W. Kenny, "What is the Young's modulus of silicon?," *Journal of Microelectromechanical Systems*, 2010, vol. 19, no. 2, pp. 229-238. doi: 10.1109/JMEMS.2009.2039697
- [10] B. A. Gama, S. L. Lopatnikov, and J. W. Gillespie Jr., "Hopkinson bar experimental technique: A critical review," *Applied Mechanics Reviews*, 2004, vol. 57, no. 4, pp. 223-250. doi: 10.1115/1.1704626
- [11] F. Yi, Z. Zhu, F. Zu, S. Hu, and P. Yi, "Strain rate effects on the compressive property and the energy-absorbing capacity of aluminum alloy foams," *Materials Characterization*, 2001, vol. 47, pp. 417-422. doi: 10.1016/S1044-5803(02)00194-8
- [12] B. Song, and W. Chen, "Split Hopkinson pressure bar techniques for characterizing soft materials," *Latin American Journal of Solids and Structures*, vol. 2, 2005, no. 2, pp. 113-152. url: <http://www.lajss.org/index.php/LAJSS/article/view/73>
- [13] A. Cao, P. L. Dickrell, W. G. Sawyer, M. N. Ghasemi-Nejhad, and P. M. Ajayan, "Super-compressible foam like carbon nanotube films," *Science*, 2005, vol. 310 no. 5752, pp. 1307-1310. doi: 10.1126/science.1118957
- [14] T. Tong, Y. Zhao, L. Delzeit, M. Ali Kashani, M. Meyyappan, and A. Majumdar, "Height independent compressive modulus of vertically aligned carbon nanotube arrays," *Nano Letters*, 2008, vol. 8, no. 2, pp. 511-515. doi: 10.1021/nl072709a
- [15] S. B. Hutchens, A. Needleman, and J. R. Greer, "Analysis of uniaxial compression of vertically aligned carbon nanotubes," *Journal of the Mechanics and Physics of Solids*, vol. 59, no. 10, pp. 2227-2237, 2011. doi: 10.1016/j.jmps.2011.05.002



Investigating the Unrecovered Displacement of Glass Fibre Reinforced Polymers Due to Manufacturing Conditions

M. SHAH MOHAMMADI, L. SOLNICKOVA, B. CRAWFORD, M. KOMEILI and A. S. MILANI*

Composites Research Network—Okanagan Node, School of Engineering, University of British Columbia, Kelowna, BC, V1Y 1V7, Canada

KEYWORDS

polymer composites
open moulding
process conditions
creep
unrecoverable deformation

ABSTRACT

In this industrial case study, the effect of processing conditions on the cure progression as well as the magnitude of creep strain due to storage/post-operations after de-moulding was investigated via a wet lay-up manufacturing of a glass fibre reinforced polymer (GFRP), commonly used in boat building. In addition, how the creep and the related permanent deformation in its recovery stage can be prevented or controlled was a focus of the study. Dynamic Mechanical Analysis (DMA) was used to monitor the creep rate of test samples while a constant stress was applied to mimic the sagging condition of GFRP parts during assembly stages. Differential Scanning Calorimetry (DSC) was used to determine the degree of cure as well as the glass transition temperature (T_g) at different curing temperatures. A direct relationship was found between the curing and the operating temperatures, and the unrecovered displacement seen in the final GFRP part. The unrecovered displacement was hypothesized to occur mainly due to a combination of cure progression and creep during the manufacturing process. Namely, cure progression results in the development of stiffness retaining the elastic deformation, while creep can create irreversible viscous flow. The results obtained may be particularly helpful to manufacturers of open moulded parts to prevent the costly consequence from excessive recurring of parts after de-moulding.

© 2014 DEStech Publications, Inc. All rights reserved.

1. INTRODUCTION

Light weight, high specific stiffness/strength and lower thermal expansion of Glass Fibre Reinforced Polymers (GFRPs) have led to their widespread applications in many industries including marine, automotive, sporting and civil [1]. The time-temperature-cure dependent behaviour is an important consideration in the design and analysis of structures made of FRP materials since polymer resins exhibit thermo-viscoelastic behaviour [2], which has a major impact on the effective mechanical behaviour of final parts [3]. This dependence is significantly affected by various conditions (e.g., environmental conditions, processing time and temperature, etc.) [4]. In addition, creep, a relatively slow,

progressive deformation under constant load [5] can occur in viscoelastic materials and cause irreversible dimensional changes during manufacturing (e.g., undesired time-dependent deformation in GFRP parts under their own weights during assembly stages).

The present article is from a case study performed in the recreational boat industry. Boats made of GFRP composites are manufactured in two specific parts (deck and hull). Each part is usually left on a storage rack after de-moulding and before the boat is assembled and transferred. In this post-moulding stage, the part may experience a load over a period of time due to, for example, self-weight (sagging), or external loads, and start deforming undesirably. Therefore, creep could be a non-negligible contributing factor to the process-induced deformation of such large GFRP parts [6]. Consequently, the hull and deck parts may not hold to the pre-specified geometric tolerances to fit together, which in

*Corresponding author. E-mail: abbas.milani@ubc.ca

turn can cause considerable problems during assembly. The extent to which the creep, as well as the associated permanent deformation in its recovery stage, can be prevented or controlled by processing conditions has been the focus of the presented work via a set of designed experiments as follows.

2. EXPERIMENTAL PROCEDURE

Initially, wet lay-up technique was used to prepare a plate sample (300 mm × 900 mm) consisting of three fibre-glass mat layers and unsaturated polyester resin (Aropol®, Ashland chemicals) initiated with 1.75% Luperox DDM-9 initiator for a total thickness of approximately 2 mm. This laminate was left to cure past the gelation point, enough to de-mould and then quickly transferred to a freezer to preserve minimal cure. The fibre content of the fabricated composite laminate was determined to be 48 ± 0.35 wt% from the resin burn-off experiment. 15 mm × 60 mm specimens were cut from the master plate using a table saw. Six batches of nine small specimens were placed into an environmental chamber at 10, 20, 30, and 40°C for 180 minutes where a cure plateau was reached for each batch. Then, each batch was moved back to the freezer to preserve its final degree of cure.

Two specimens from each specific conversion batch were tested using a three-point bending clamp of a Dynamic Mechanical Analyzer (DMA-Q800). One temperature condition imitated the summer ambient temperature (30°C) and the second temperature condition imitated the winter condition (10°C) on the manufacturing floor in Kelowna BC, Canada. Three repeats per temperature (i.e., from each batch) were performed. The DMA was used to monitor the creep rate of each test sample while a constant stress is applied, following ASTM D2990. In order to properly capture the creep behaviour of the material, a corresponding relaxation period of 30 minutes was applied after the loading. Then, the load was removed and the recovery behavior of the samples was monitored. The magnitude of applied force (1.2 N) was chosen based on self-weight and the second moments of area scaled from an industrial part to induce the maximum normal stress equivalent to that during part storage.

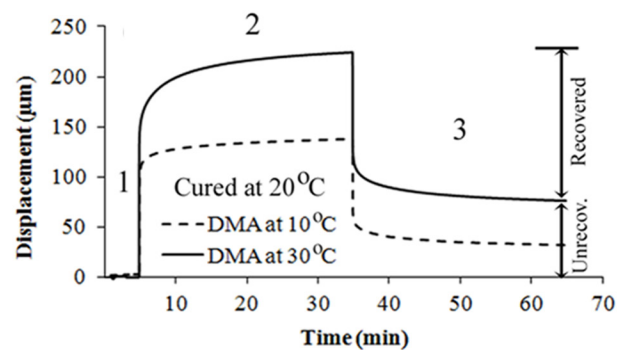
The degree of cure of each testing condition was analyzed using Differential Scanning Calorimetry (DSC-Q2000, TA Instruments). This was conducted by comparing the residual heat of reaction evolved from the sample ($\Delta H_{\text{residual}}$) to the total heat of reaction of completely uncured raw resin (ΔH_{Total}) [Degree of cure = $1 - \Delta H_{\text{residual}}/\Delta H_{\text{Total}}$] [7].

3. RESULTS AND DISCUSSION

The creep representative curves of the GFRP laminates, depicting the change in displacement over time under the specified operating temperature and loading conditions (Figure 1), confirmed that creep for the given material is tem-

perature-dependent. Additionally, for the same part, cured at 20°C, there is an increase in the creep displacement at the higher temperature; for example when the post-moulding operation or in-service loading is applied in summer. This is because of a temperature increase during the storage period after de-moulding leading to a greater degree of the polymer chains mobility by means of a higher molecular kinetic energy. In addition, the material becomes softer and flows more readily at higher temperatures, owing to the greater influence of the viscous component of partially cured resin. On the other hand, at a given operating temperature, the creep-induced displacement magnitude after de-moulding is seen to considerably decrease by increasing the curing temperature of the resin during the moulding process [Figure 1(b)].

Figure 2(a) shows representative DSC thermographs. The heat of reaction was significantly smaller for the partially cured samples compared to that of the raw resin. There was also a sequential reduction in the heat of reaction as the curing temperature increased due to a progressive increase in



1: Initial Elastic Response, 2: Transition Region, 3: Recovery
(a)

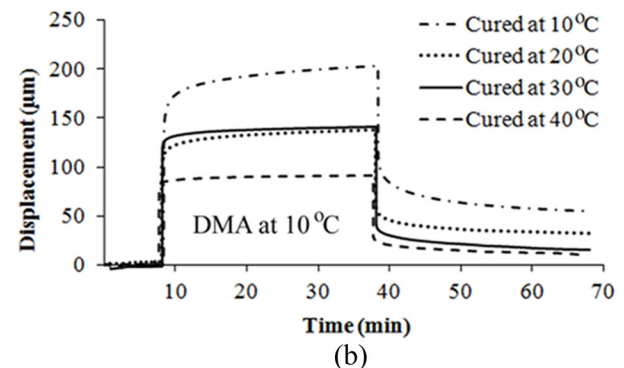


Figure 1. Representative curves illustrating the behaviour of the specimens under creep test using DMA at different operating (DMA) temperatures but the same cure state (a), and same operating (DMA) temperature but different curing temperatures (b). Total and unrecovered displacements was higher at the higher operating temperature (30°C) compared to the lower operating temperature (10°C) at a constant curing state. An increase in the curing temperature resulted in considerable reduction in total and unrecovered displacements at a constant operating temperature.

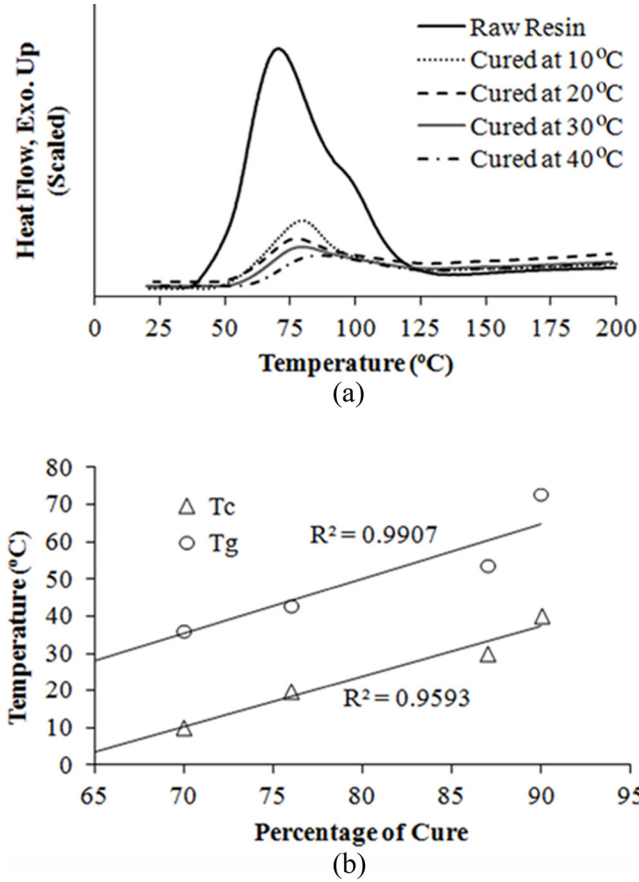


Figure 2. (a) Representative DSC thermographs illustrating the exothermic curing reaction for different resin samples pre-cured at 10, 20, 30 and 40°C, as well as the raw resin. The significant reduction in the heat of reaction of the pre-cured samples compared to the raw resin indicated the increase in the degree of cure as the curing temperature increased. (b) Curing temperature (T_c), and glass transition temperature (T_g) versus degree of cure. As can be seen, the degree of cure increased by increasing the curing temperature. A linear correlation between T_c , T_g and degree of cure was observed. It was found that an approximately 25°C temperature difference between T_c and T_g existed once cure progression had stopped for all the curing temperatures (adapted from [9]). (Note: T_g of -67°C, which is the T_g of the raw resin (degree of cure = 0), has been considered in the plot.).

the initial cure extent, and hence, less un-reacted resin material was available to participate in the curing reaction during the DSC heating cycle (4°C/min). There was a linear correlation between T_c and T_g , as well as each with the degree of cure [Figure 2(b)]; e.g., the degree of cure increased by increasing the curing temperature T_c ; similarly there was an increase in the glass transition temperature T_g as the cure progressed. Interestingly, there was almost a constant difference (about 25°C) between T_c and T_g at each degree of cure. This temperature difference is a critical practical threshold value and specific to each given resin type [8]. It has been acknowledged that cure predominately stops when: $T_g - T_c \geq \text{critical value}$; for a given steady cure state, raising T_c will lower $T_g - T_c$ below the critical value and cure

can then continue and raise T_g . As the curing temperature was increased from 10°C to 40°C, a statistically significant reduction in the unrecovered displacement was observed under a given operation temperature [Figure 3(a)]. Also, there was a statistically significant reduction in the unrecovered displacement at lower operating temperature, given the same initial curing temperature.

Figure 3(b) shows unrecovered creep displacement values plotted versus $T_g - T_{\text{Operation}}$ (where $T_{\text{Operation}}$ now replaces T_c as the new temperature due to the DMA condition; i.e., post-moulding operation temperature). It was found that both the initial curing temperature, which directly alters T_g right before de-moulding, and the operating temperature influencing the creep displacement, affect $T_g - T_{\text{Operation}}$ and result in a concomitant reduction in the unrecovered (per-

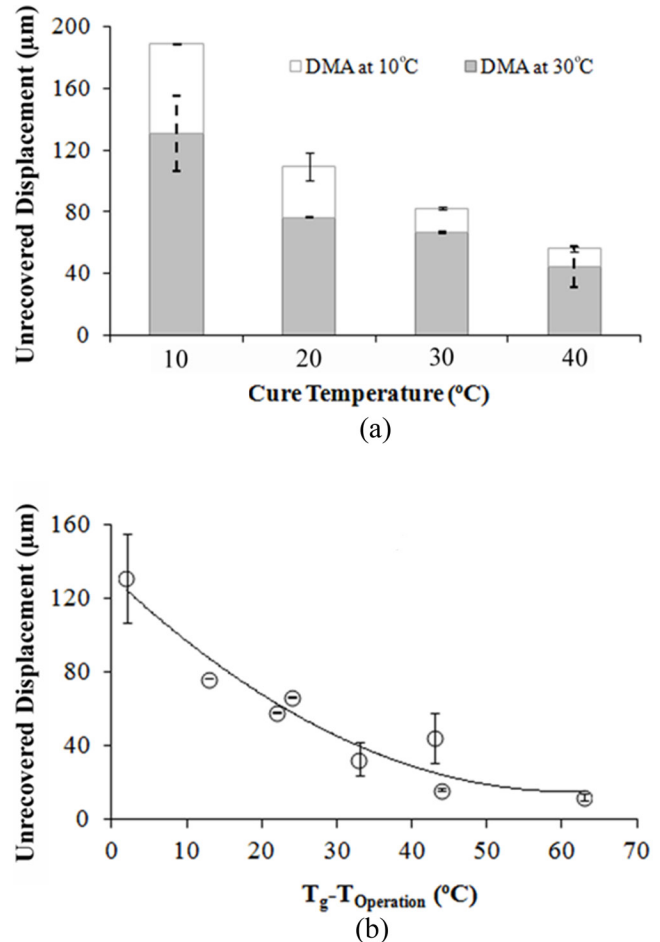


Figure 3. (a) Unrecovered displacement dependencies on curing temperature upon load removal. There were statistically significant differences between all pairs of sample means with a significance level of $p < 0.05$ according to Paired *t*-test. (b) Unrecovered displacement dependency on $T_g - T_{\text{Operation}}$. Final unrecovered displacement was dependent on both curing temperature (affecting T_g) and operating temperature. There was a continuous reduction in the unrecovered displacement as the $T_g - T_{\text{Operation}}$ increased; hence, both curing and operating temperatures contribute to the unrecovered displacement (Adapted from [9]).

manent) displacement; i.e., if parts are not cured enough in the mould, then T_g will be too low before de-moulding. In this case, parts that are stored after de-moulding, then transported or generally operated at high temperatures, may get too close to T_g and become soft enough to undergo a notable deformation under a given load. Therefore, in manufacturing of composite parts, transportation, storage and operating temperatures of the parts must be considered based on the T_g of the parts dictated by the curing temperature. In addition, when $T_g - T_{\text{Operation}}$ is lower than the critical value, for example at low T_g and high operating temperature, cure can still progress. Consequently, the elasticity of the part increases and the elastic displacement that had occurred upon loading will not be fully recoverable.

4. CONCLUSIONS

A direct relationship between the curing, glass transition, as well as operating temperatures and the unrecovered displacement that may occur during transportation, storage or operation of composite parts was found. It was hypothesized that this unrecovered displacement was mostly attributed to a combination of cure progression and creep which results in a partial recovery of the total displacement. Cure progression leads to the development of stiffness that retains the elasticity, while creep can cause irreversible viscous flow. Consequently, undesired dimensional changes occur when the part is removed from the mould after partial curing and transported or stored at a temperature that is close enough to the T_g of the part. Therefore, the part is softened to the point at which has the potential to undergo creep under the applied loads; e.g., its own weight when stored on a storage structure. It was also found that there is about 25°C difference between the curing temperature and the resulting T_g (in the case of Aropol[®] unsaturated polyester resin used in the case study). The part has the potential to become soft and also to further cure and change the T_g at temperatures within this window. Thus, the operation and storage temperatures should be ideally low enough, compared to the curing temperature, to make sure that the part neither further cures, nor exhibit a notable viscous behaviour.

5. ACKNOWLEDGEMENT

The Authors would like to thank Campion Marine Inc. and FormaShape Inc. for their in-kind contributions in this research. Thanks are also due to other colleagues in the Composites Research Network (CRN), particularly Dr. Christophe Mobuchon, for their helpful feedback. In addition, financial supports from the Western Diversification Canada (WD) and Natural Sciences and Engineering Research Council (NSERC) of Canada are greatly acknowledged.

6. REFERENCES

- [1] Mair R. I.: Fibre Reinforced Polymers—From Aerospace to Infrastructure. ATSE (Australian Academy of Technological Sciences and Engineering) Focus, No 107, 5–6/99 (1999).
- [2] Chartoff R. P., Menczel J. D., Dillman S. H.: Dynamic Mechanical Analysis (DMA). In: Thermal Analysis of Polymers: Fundamentals and Applications (eds.: Menczel J. D., Prime R. B.), John Wiley and sons Inc., Hoboken, NJ (2009). <http://dx.doi.org/10.1002/9780470423837.ch5>
- [3] Aboudi J., Cederbaum G.: Analysis of viscoelastic laminated composite plates. *Composite Structures*, 12 (4), 243–256 (1989). [http://dx.doi.org/10.1016/0263-8223\(89\)90074-3](http://dx.doi.org/10.1016/0263-8223(89)90074-3)
- [4] Touati D., Cederbaum G.: Stress Relaxation of Nonlinear Thermoviscoelastic Materials Predicted from Known Creep. *Mechanics of Time-Dependent Materials*, 1, 321–330 (1998). <http://dx.doi.org/10.1023/A:1009759205294>
- [5] Bair H. E., Akinay A. E., Menczel J. D., Prime R. B., Jaffe M.: Thermomechanical analysis (TMA) and Thermodilatometry (TD). In: *Thermal Analysis of Polymers: Fundamentals and Applications* (eds.: Menczel J. D., Prime R. B.), John Wiley and Sons Inc., Hoboken, NJ (2009). <http://dx.doi.org/10.1002/9780470423837.ch4>
- [6] Sperling L. H.: Introduction to Physical Polymer Science. John Wiley and Sons Inc, NY, (2005). <http://dx.doi.org/10.1002/0471757128>
- [7] Sadeghinia M, Jansen K.M.B., Ernst L.J.: Characterization of the viscoelastic properties of an epoxy molding compound during cure. *Microelectronics Reliability*, 52, 1711–8 (2012). <http://dx.doi.org/10.1016/j.microrel.2012.03.025>
- [8] Pascault J. P., Sautereau H., Verdu J., Williams R. J. J.: Glass Transition and Transformation Diagrams. In: *Thermosetting Polymers* (ed.: Hudgin D. E.), Marcel Dekker, Inc., New York, NY (2002). <http://dx.doi.org/10.1201/9780203908402.ch4>
- [9] Shah Mohammadi M., Solnickova L., Crawford B. J., Komeili M., Milani A. S.: A case study on dimensional change of glass fibre reinforced polymers after demoulding: A combined effect of cure progression and thermo-viscoelastic behaviour. *19th International Conference on Composite Materials, Montreal, Canada* (2013).



Experimental Ballistic Response and Modeling of Compound Structures Based on Textile Fabrics

LIONEL GILSON^{1,*}, JOHAN GALLANT², FREDERIK COGHE² and LUC RABET¹

¹Department of Civil and Materials Engineering, Royal Military Academy, 30 avenue de la Renaissance, 1000 Brussels, Belgium

²Department of Weapon Systems and Ballistics, Royal Military Academy, 30 avenue de la Renaissance, 1000 Brussels, Belgium

KEYWORDS

IED
modeling
ballistic
impact, textile

ABSTRACT

This paper summarizes the ballistic considerations of a general project concerning the protection against the threats associated with improvised explosive devices (IEDs). IEDs generate two kinds of threats: blast and fragments. One possible protection combines a ballistic textile (Kevlar[®]) to stop the fragments and a crushable material (Crushmat[®]) for absorbing the blast. In order to properly develop an optimized protection, the different materials were tested separately before combining them. Numerical models were also developed with DYNAFAB[®] and LS-DYNA[®] in order to determine and optimize the relevant design parameters. Good correlations were obtained between the models and the experiments. The investigated combined protection system could serve as an interesting basis against more general terrorist threats like fragmentation bombs. The evolution of computer resources will allow modeling such complex assemblies of materials with more details and reduce the calculation time.

© 2014 DEStech Publications, Inc. All rights reserved.

1. INTRODUCTION

The use of fabric armor in certain ballistic applications is increasingly preferred over conventional rigid metal armor systems because of its superior strength-to-weight ratio and flexibility. To date, the design and development of such fabric armor systems have largely been approached empirically. Impact tests and empirical quantities such as V50 are used primarily as gauges to benchmark the ballistic performance of different materials. Research on dynamic behavior of textile materials under impact is a relatively new area of interest. As the need to manufacture a light and effective personal protective system grows, the need to develop an accurate and robust design tool increases.

Many efforts have been directed in the past to study the dynamic behavior of textile materials under impact. Initially, most of the studies focused on mathematical modeling of single yarns, which are the main constituents of fabrics, un-

der transverse impact [1–4]. Analytical models were developed from the knowledge obtained during the study of single yarns to predict the behavior of fabrics under impact [4–6]. Due to the geometrical complexity of a fabric, many of the analytical solutions failed to capture the response of a fabric with an acceptable accuracy. The introduction of personal computers guided many researchers toward simulating the impact using numerical models [7–22]. Different models were suggested, but due to lack of experimental knowledge, none of them has been properly verified. Most of the experimental studies are limited to measuring the striking and residual velocity of the projectile, without providing any data during the impact event. Photographic investigations are also performed to visualize the deformation characteristics of a fabric during impact, which provide a limited set of data for the displacements within the impact duration. However, there has always been a desire to capture the on-going response of the target and projectile deceleration during the impact.

Moreover, in a lot of practical applications, it is necessary to combine an anti-blast protection with a ballistic protection

*Corresponding author. E-mail: lionel.gilson@rma.ac.be, Tel : +32 2 742 6420, Fax : +32 2 742 6412

when the threat is, for example, an improvised explosive device (IED) which generates not only fragments but also a blast wave. The effects of the latter must be decreased in order to protect the person or structure. Cellular and granular materials are usually used against explosion effects. However, there is little quantitative knowledge about the dynamic behavior of these materials and, before integrating such an anti-blast material into a protection, studies on the performance of these materials are essential. Although a thorough, quantitative understanding of all the mechanisms that occur during ballistic impact into fabrics and compliant laminates, and blast absorption by cellular materials does not exist yet, much has been learned through experimental observations and analysis of modeling efforts.

The aim of this project is to study how a protective structure made of an anti-blast material and a textile based ballistic protective material will be able to resist ballistic impact (the problem of the blast wave will not be discussed here). Different materials and configurations will be tested by real experiments or evaluated using numerical methods. The work hence aims to obtain a better understanding of the mechanisms improving the capability of the combined protection (blast and impact threats) to stop an incoming projectile. This paper describes the development of a combined protection in three separate steps for the two best materials studied in the framework of this research.

2. FIRST STEP: THE TEXTILE

2.1. Experimental

In order to test the resistance of the fabric against ballistic

impact, several tests were performed on textile layers of 40×40 cm. The experimental set-up consists of a 10 GHz Doppler radar, a 26 GHz Doppler radar, a high speed camera and a double optical basis. Projectiles are 6.5 mm steel balls that showed no deformation after impact. Figure 1 summarises the configuration of the experimental set up used for the tests.

The originality of these tests is the measurement of the evolution of the projectile speed during penetration of the target using the 26 GHz Doppler radar. Next to this, the high-speed camera allows observing the impact time, the deformation history of the cone created during impact and penetration of the projectile, and, when perforation occurs, the perforation time. The 10 GHz Doppler radar measures the projectile velocity before impact. The optical basis is used as a trigger for the measurement system and a double-check for the 10 GHz Doppler radar.

2.2. Modeling

The rapid development and great variety of textile materials on the market have promoted experimental research about their impact performances [12,23]. However, these experimental approaches are often complicated because of the high-speed phenomenon. These tests often give only information about apparent characteristics like projectile displacement or impact and residual velocity. The main advantage of numerical simulations is the possibility for description and observation of failure mechanisms.

Several ways can be used to perform impact simulations of textile materials. Duan *et al.* [24] developed a textile model based on woven solid elements. Such a model is able to

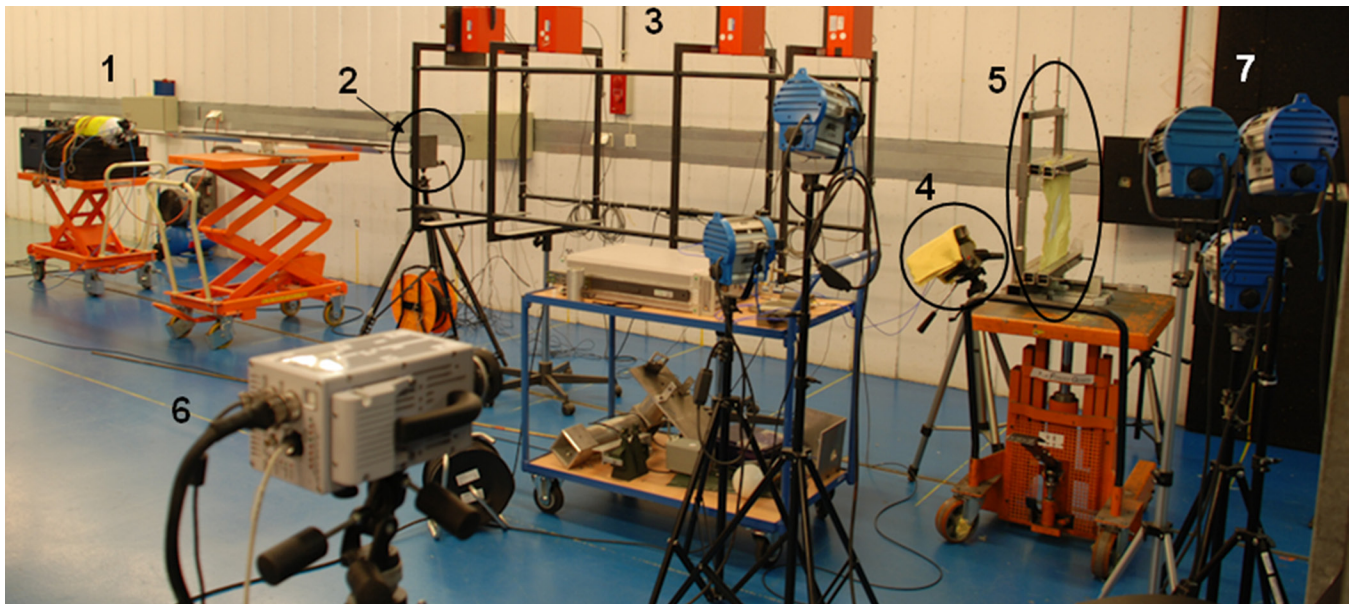


Figure 1. Experimental setup: (1) gas gun, (2) Doppler radar, (3) optical basis, (4) Radar 26 GHz, (5) tested sample, (6) high speed camera, (7) additional lighting.

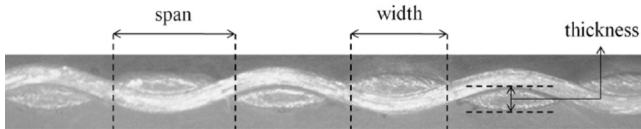


Figure 2. Micrograph of a typical section of Kevlar[®] and the relevant dimensions of such a structure [14].

describe the impact response of textile materials for different projectile velocities [25]. Other models consider the textile as a homogenous bi-dimensional shell. This is the case e.g. of Roylance et al [5] and Shim *et al.* [26]. Finally, a hybrid method between the two aforementioned exists too. This is the hybrid element analysis as described by Nilakantan and Rao [14,27].

For the applications considered here, the full woven solid element approach was preferred because of its precision especially at the impact point during penetration and perforation. All the modelled fabrics are generated with DYNAFAB[®] [16] and imported into LS-PrePost[®].

DYNAFAB[®] is interesting because it allows generating geometries and meshes for textiles in a fairly simple way before importing them in LS-PrePost[®]. The geometries of the yarns can be easily obtained by microscopic measurements of the typical dimensions of the yarns in the considered fabric (Figure 2). Table 1 summarizes the dimensions of the Kevlar[®] fabric that was used in this study.

The boundary conditions must be carefully selected. Ideally, these boundary conditions have to mimic these of the experiments. However, if the available boundary conditions are free edge or full blocked edge, the model is not representative since in reality, a textile material can never be perfectly fixed in a frame. When an edge is fixed, a perfect fixing or clamping of the edge in the frame during the experiments is hence implicitly assumed. In the tests and simulations performed for this research, two edges were fixed (upper and lower), while the two other are free. For the numerical simulations an impact at the center of the fabric by a rigid spherical projectile is considered. The symmetry of this configuration allows reducing the size of the model and to model only a quarter of the structure (Figure 3). The square fabric model has edges with a length of 20 cm. However, for such a geometry and meshing, the quantity of data is too high and needs to be simplified. The size of the modeled tissue was reduced to 25 mm. A simple elastic material model with erosion was

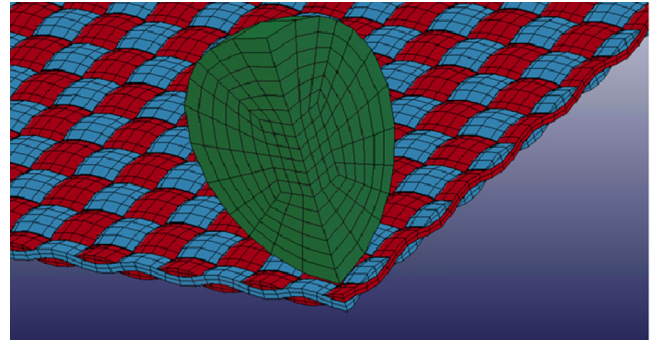


Figure 3. View of the fully woven solid element model with the symmetry for one layer of Kevlar[®] generated with DYNAFAB[®] and imported in LS-PrePost[®].

used to represent the properties of Kevlar[®] ($\rho = 1310 \text{ kg/m}^3$, $E = 62 \text{ GPa}$ and $\sigma_{\max} = 2.3 \text{ GPa}$) [14,25].

The model needs to be completed with a correct contact definition. For the simple impact problem, an AUTOMATIC-SURFACE-TO-SURFACE contact was used. In LS-PrePost[®], contacts are important because they allow the definition of the frictional coefficients. For this first step, the value of the frictional coefficient is not very important but needs to be greater than zero because of the spherical shape of the projectile. Indeed, with a zero value of this coefficient, a spherical projectile would slip between the yarns of the target without any rupture of fibers during its penetration, which is not realistic. A low frictional static and dynamic coefficient (0.2) was used. The literature often mentions values between 0 and 0.5 for the friction between projectile and textile materials [9,12]. This parameter becomes more important when the final models are considered (see section 4.2). The comparison between the experiments and different models showed good accordance and is extensively developed in [22].

3. SECOND STEP: THE CRUSHABLE MATERIAL

3.1. Experimental

Ballistic impact tests have been conducted on different samples of granular materials. Mainly Crushmat[®] and vermiculite were tested because of their interesting properties in terms of weight and blast absorption efficiency. In these tests, a 5.56 mm steel ball is fired at about 1200 m/s against samples of Crushmat[®] (section of $15 \times 15 \text{ cm}$). Two sample thicknesses are tested for Crushmat[®] (3 cm and 18 cm) while the thickness of the vermiculite sample was 12 cm. Entry and exit projectile velocities are measured thanks to a Doppler radar. The velocity drop of the projectile in the air is considered negligible between the measurement bases and the impact as well as after the exit from the sample. Witness sheets have also been placed in the samples in order to measure the velocity decrease during penetration. Figure 4

Table 1. Geometrical Properties of the Kevlar[®] used for the Tests and Simulations.

Kevlar [®] dimensions (mm)					
Warp			Weft		
Width	Span	Thickness	Width	Span	Thickness
1.113	1.203	0.244	1.228	1.195	0.209

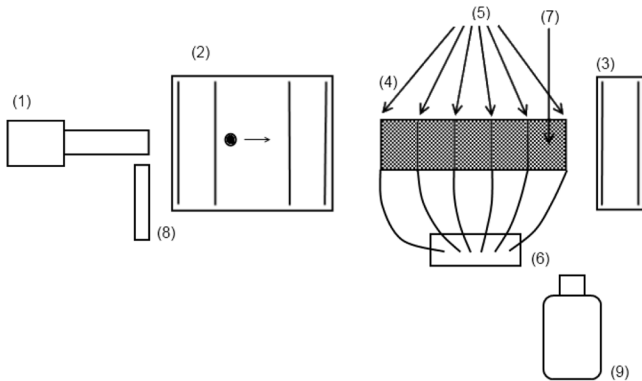


Figure 4. Overview of the setup: (1) gun, (2) optical basis as trigger of the whole measurement system, (3) optical basis to measure residual velocity after perforation, (4) tested sample, (5) trigger screens to measure velocity decrease during penetration, (6) acquisition data system for trigger screens, (7) Crushmat®, (8) Doppler radar to measure the impact velocity, (9) high-speed camera.

shows the setup for these tests. The results of the tests are summarized in Figure 5.

Comparing vermiculite and Crushmat®, Crushmat® offered the best ballistic protection. Therefore, the following modelling efforts were concentrated on this material.

3.2. Modeling

LS-DYNA® simulations are conducted in order to model the behavior of granular materials subjected to the impact of spherical rigid projectiles. The approach chosen was a simu-

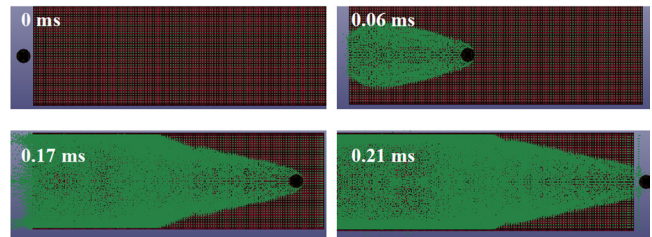


Figure 6. Simulation of the impact of a rigid sphere on Crushmat® (thickness: 12 cm).

lation based on Smooth Particles Hydrodynamics (SPH) because SPH particles can be considered as granulates and could thus be appropriate for granular material modeling. The same symmetry as for the textiles was exploited. The projectile is defined as a Lagrangian rigid body. As the SPH simulation is heavier than running a Lagrangian model, the initial front face of 15×15 cm is limited to a 4×4 cm square. The thicknesses considered were 3, 6, 9, 12, 15 and 18 cm. The particle density is set to 600 and the standard mesh is composed by $40 \times 40 \times 30$ (or 60, 90, 120, 150, and 180) particles (1 mm spacing between particles). For the contact definition between the projectile and the SPH part, an AUTOMATIC-NODE-TO-SURFACE CONTACT was chosen. For this model, an important consideration is the friction between the objects. Static and dynamic frictional coefficients were set to 1.9 (close to the maximum value permitted by LS-DYNA®) which gave the best fit between experimental and numerical residual velocities. Figure 6 shows

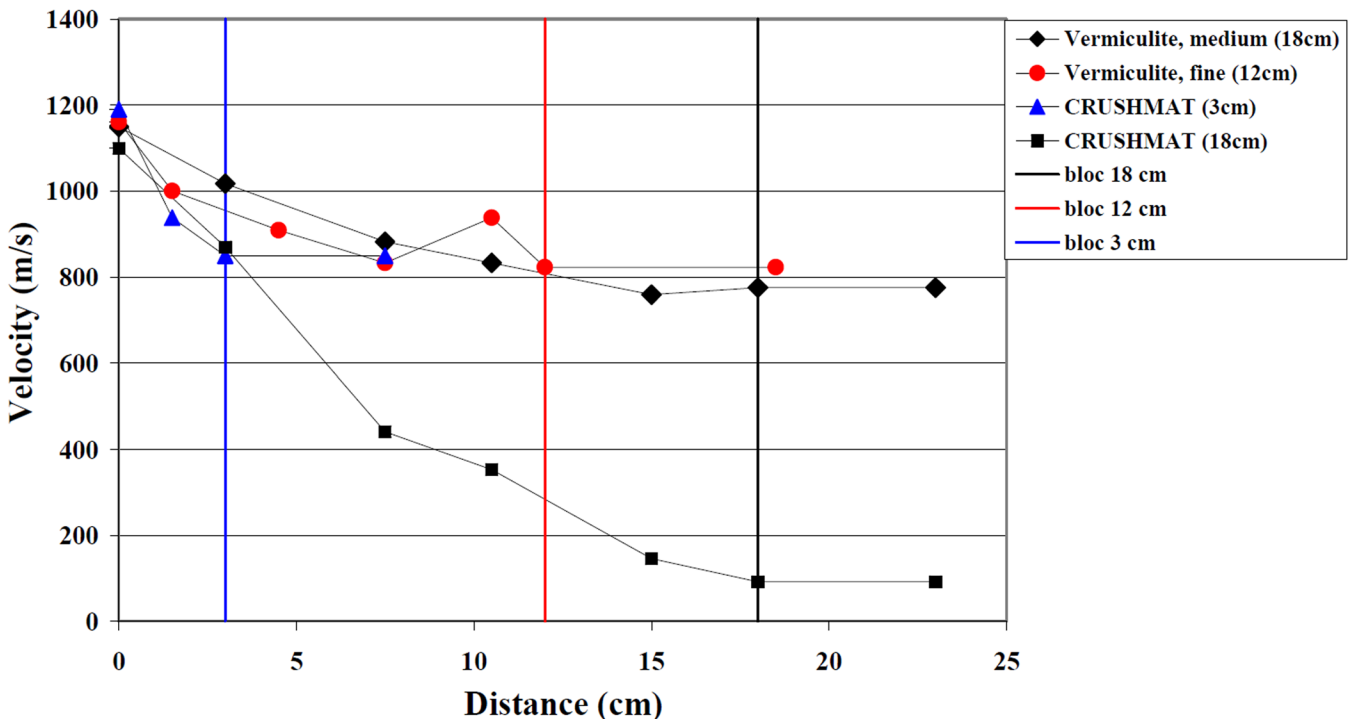


Figure 5. Velocity decrease in granular materials.

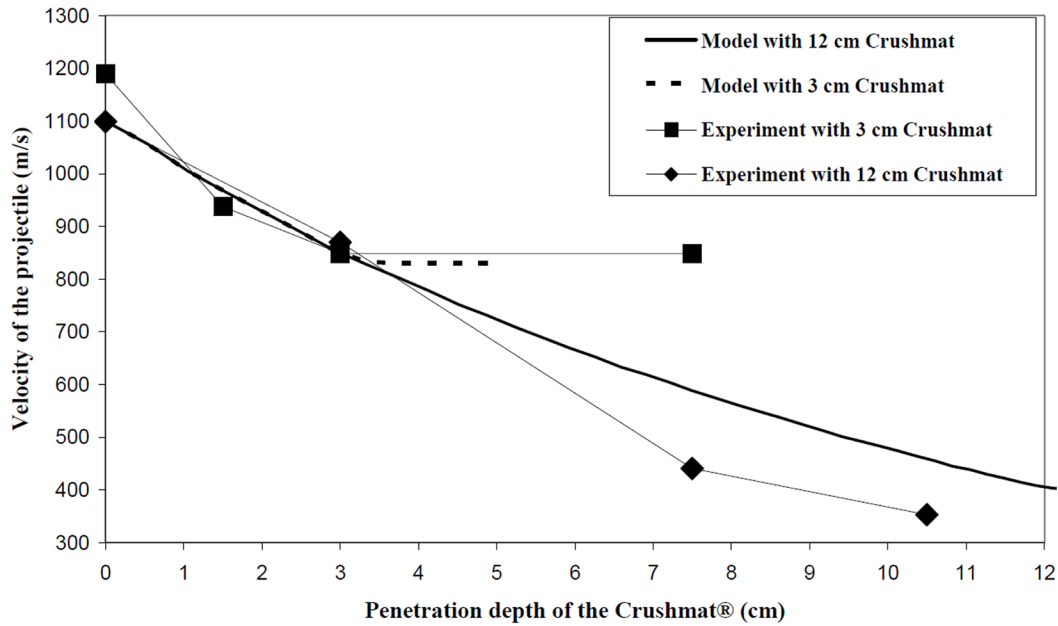


Figure 7. Experimental and numerical evolution of the projectile velocity as a function of the penetration depth in Crushmat®.

such a model for 12 cm of Crushmat®. The Crushmat® was represented by a porous material model having a density of 600 kg/m^3 (MAT_NULL card in LS-DYNA®).

4. THIRD STEP: COMBINED PROTECTION

4.1. Experimental

Rigid steel balls of 5.56 mm and 0.7 g were launched with a Sabre cannon caliber .308 using Remington .308 magnum accelerator ammunition equipped with a sabot. The velocity of the projectile is controlled by varying the powder mass in the cartridges. The velocity of the projectile before impact, during penetration and after perforation was measured by a combination of different instruments as presented in Figure 4. The sample is made of cylindrical tubes of different lengths (3, 6, 9, 12, 15 cm) which can contain different quantities of granulates and trigger screens for measuring the perforation time and, by combining the results for different triggers screens, the velocity decrease of the projectile in between two sequential screens. Kevlar® layers are inserted at the front and at the back of the tube (1, 2 or 3 layers in front and 2, 3 or 5 layers at the back), as shown in Figure 8.

4.2. Modeling

The numerical model (Figure 9) was developed with LS-PrePost®. The Kevlar® was modeled in the same way as described in section 2.2. The Crushmat® was represented as described in section 3.2.

An AUTOMATIC-SURFACE-TO-SURFACE contact

was chosen to model the contacts between the different Lagrangian solids. For the contact between the SPH nodes and the Lagrangian solids a NODE-TO-SURFACE contact was chosen. The friction between the different materials is especially important when considering bodies in contact with the Crushmat® material. This can be seen in Figure 10, where one can observe a great pull-out of yarns from the Kevlar® layers at the back of the protection.

In order to take into account this high friction due to the presence of pulverized Crushmat® particles in the sample, a

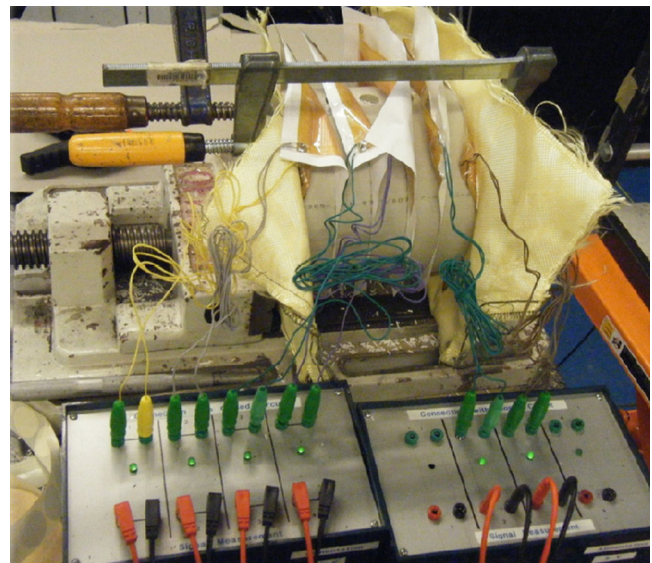


Figure 8. Target system, composed of a tube filled with granular material, textile layers at the front and at the back, and trigger screens in between.

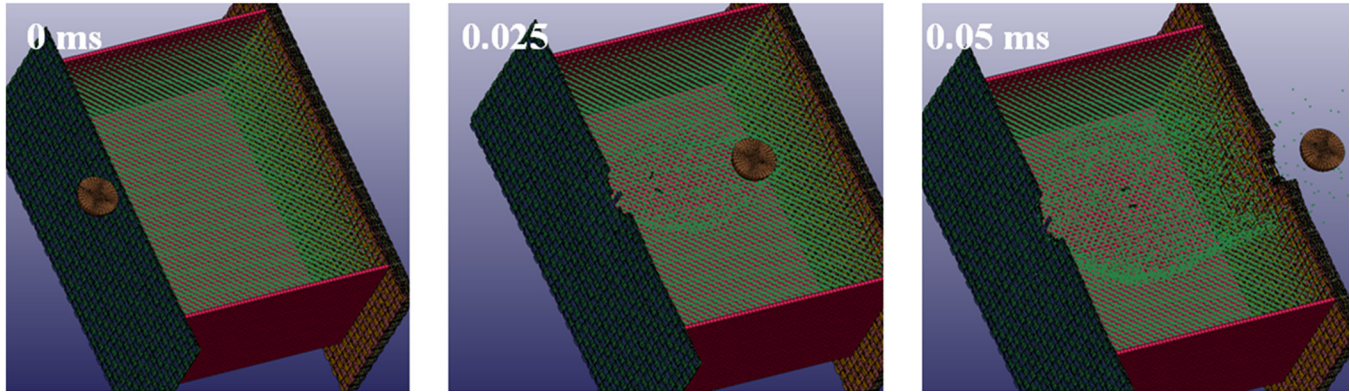


Figure 9. Numerical model of sphere impact on Kevlar® (one layer in front and five at the back) and 3 cm Crushmat®.

high frictional coefficient was chosen in the simulations (set to 1.9). Some parts represented by Lagrangian solids in the simulations are however not in contact with this pulverized Crushmat® (for example the front layer of Kevlar® when impacted by the projectile). Accordingly, the frictional coefficient is set to 0.2 as described in section 2.2.

Figure 11 shows a comparison between experimental results and the simulations showing reasonable agreement in terms of residual velocities. However, more detailed studies should be realized in order to take into account of the statistical nature of the ballistic phenomena and for a refinement of the different parameters of the used material models.

Moreover, Figure 11 shows that the residual velocity is generally substantially larger in the case of five Kevlar® layers at the back of the sample, than for three Kevlar® layers. This result seems counterintuitive, but both the experiments and the simulations exhibit the same phenomenon. Future work will focus on this.

5. CONCLUSION

The aim of this work is to investigate on possible new approaches to develop a combined protection system against threats generating both blast effects and fragments. A specific combination of two materials was selected in the framework of this project, which should be able to absorb both these threats: a ballistic textile (Kevlar®) against fragments and a granular material (Crushmat®) against blast. By combining these materials, synergies might exist e.g. the contribution of the blast-absorbing material to an increased deceleration of the fragments (represented by the steel balls). A suitable experimental setup was developed in order to test these materials both separately and combined into a single system. These experiments allowed observing the different phenomena during the penetration and perforation processes of the targets. The most relevant information coming from the experiments are the effects of the friction on the deceleration of the projectile during penetration and the increased



Figure 10. Illustration of the importance of the friction between the pulverized Crushmat® material and the spheres—Increased yarn pull-out and retention effect on the projectile.

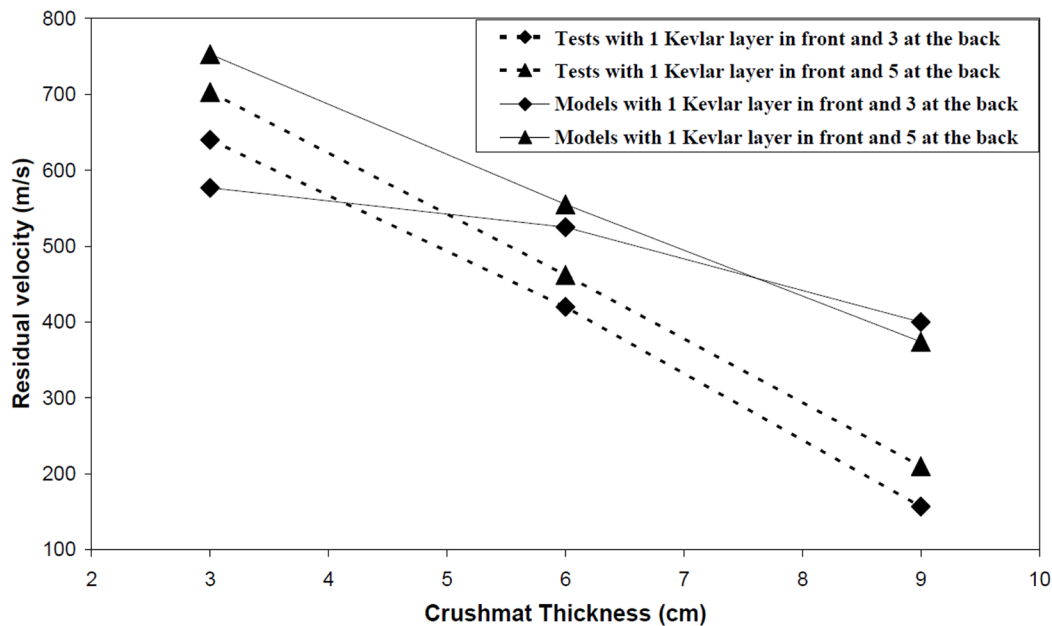


Figure 11. Comparison between experimental results (one shot for each sample) and simulations of the performance of the combined protective structures (Kevlar® and Crushmat®).

yarn pull-out effect by the presence of the granulate material when complete perforation occurs. Corresponding numerical models were developed with LS-DYNA® in order to mimic the tests and to identify the relevant parameters. A more statistical ballistic study of such combined protections is however deemed to be necessary in order to take into account the strong statistical nature of the ballistic impact phenomena, especially for complex target configurations. Finally, as it is still difficult to represent the complex reality of the penetration and perforation phenomena occurring close to the projectile, the numerical models should be refined. This would allow taking into account phenomena like the yarn pull-out and the structure of the extrusion-like deformation occurring at the back face of the protection.

6. REFERENCES

- [1] A. Shahkarami Noori, A numerical investigation of ballistic impact on textile structures, Master's thesis, Sharif University of Technology, 1995.
- [2] D. Roylance, Wave propagation in a viscoelastic fibre subjected to transverse impact, *Journal of Applied Mechanics*, pp. 143–148, March 1973. <http://dx.doi.org/10.1115/1.3422914>
- [3] J. C. Smith, F. L. McCrackin, and H. F. Schiefer, Stress-Strain Relationships in Yarns Subjected to Rapid Impact Loading : Part III. Effects of wave propagation, *Textile Research Journal*, vol. 25, pp. 701–708, August 1955. <http://dx.doi.org/10.1177/004051755502500805>
- [4] B. Parga-Landa and F. Hernandez-Olivarez, An analytical model to predict impact behaviour of soft armours, *International Journal of Impact Engineering*, vol. 16, no. 3, pp. 455–466, 1995. [http://dx.doi.org/10.1016/0734-743X\(94\)00054-Z](http://dx.doi.org/10.1016/0734-743X(94)00054-Z)
- [5] D. Roylance and S.-S. Wang, Penetration Mechanics of Textile Structures. NATICK/TR-80/021. Clothing, Equipment and Materials Engineering Laboratory, Natick, Massachusetts, United States, June 1979.
- [6] N. Naik, P. Shirao, and R. B.C.K., Ballistic impact behaviour of woven fabric Composites: Formulation, *International Journal of Impact Engineering*, vol. 32, pp. 1521–1552, 2006. <http://dx.doi.org/10.1016/j.ijimpeng.2005.01.004>
- [7] C. Lim, V. Shim, and Y. Ng, Finite-element modeling of the ballistic impact of fabric armor, *International Journal of Impact Engineering*, vol. 28, pp. 13–31, 2003. [http://dx.doi.org/10.1016/S0734-743X\(02\)00031-3](http://dx.doi.org/10.1016/S0734-743X(02)00031-3)
- [8] M. Rao, G. Nilakantan, K. B.M., B. Powers, and B. T.A., Global/local modeling of ballistic impact onto woven fabrics, *Journal of Composite Materials*, vol. 43, pp. 445–467, 2009. <http://dx.doi.org/10.1177/0021998308097684>
- [9] B. R. Scott and C.-F. Yen, Analytic design trends of fabric armor, in *Proceedings of the 22nd International Symposium on Ballistics*, pp. 752–760, 2005.
- [10] B. Cheeseman, C. Yen, B. Scott, B. Powers, T. Bogetti, B. LaMattina, Y. Duan, M. Keefe, Y. Miao, and Y. Wang, From Filaments To Fabric Packs Simulating The Performance Of Textile Protection Systems. U.S. Army Research Laboratory, Aberdeen Proving Ground, MD, United States, November 2006.
- [11] P. M. B. S. Chian Yen, Tusit Weerasooriya and B. Cheeseman, Experimental validation of a kevlar fabric model for ballistic impact, in *Proceedings of the 24th International Symposium on Ballistics*, 2008
- [12] C.-F. Yen, B. Scott, P. Dehmer, and B. A. Cheeseman, A comparison between experiment and numerical simulation of fabric ballistic impact, in *Proceedings of the 23rd International Symposium on Ballistics*, 2007.
- [13] G. Blankenhorn, K. Schweizerhof, and H. Finckh, Improved Numerical Investigations of a Projectile Impact on a Textile Structure, in *Proceedings of the 4th European LS-DYNA Users Conference*, 2003.
- [14] G. Nilakantan, M. Keefe, T. A. Bogetti, R. Adkinson, and J. W. G. Jr., On the finite element analysis of woven fabric impact using multiscale modeling techniques, *International Journal of Solids and Structures*, vol. 47, pp. 2300–2315, 2010. <http://dx.doi.org/10.1016/j.ijsolstr.2010.04.029>
- [15] G. Bohong, Ballistic Penetration of Conically Cylindrical Steel Projectile into Plain woven Fabric Target A Finite Element Simulation, *Journal of Composite Materials*, vol. 38, no. 22, pp. 2049–2074, 2004. <http://dx.doi.org/10.1177/0021998304044776>

- [16] G. Nilakantan, DYNAFAB®: User Manual. 2010. [Online]. Available: <http://www.nicomposites.com/>. [Consulted on 10 Feb 2011].
- [17] University of Nottingham, Texgen. [Online]. Available: http://texgen.sourceforge.net/index.php/Main_Page. [Consulted on 09 Jan 2014].
- [18] L. Bresciani, A. Manes, and M. Giglio, Analytical and numerical models for ballistic impacts against plainwoven fabrics with composite fibers and polymeric matrix, *Lightweight Armour Group*, 2013.
- [19] Y. Wang, Y. Miao, D. Swenson, C. B.A., C.-F. Yen, and L. B., Digital element approach for simulating impact and penetration of textiles, *International Journal of Impact Engineering*, vol. 37, pp. 552–560, 2010. <http://dx.doi.org/10.1016/j.ijimpeng.2009.10.009>
- [20] G. Nilakantan, Filament-level modeling of Kevlar KM2 yarns for ballistic impact studies, *Composite Structures*, vol. 104, pp. 1–13, 2013. <http://dx.doi.org/10.1016/j.compstruct.2013.04.001>
- [21] G. Nilakantan, M. Keefe, T. A. Bogetti, and J. W. G. Jr., Multi-scale modeling of the impact of textile fabrics based on hybrid element analysis, *International Journal of Impact Engineering*, vol. 37, pp. 1056–1071, 2010. <http://dx.doi.org/10.1016/j.ijimpeng.2010.04.007>
- [22] L. Gilson, J. Van Roey, J. Gallant, and L. Rabet, A comparison of different methods for the simulation of ballistic impacts on textile structures. *Personal Armour System Symposium*, 2012.
- [23] N.Naik, S.Borade, M. Sailendra H. Arya, and S. Prabhu, Experimental Studies on Impact Behaviour of Woven Fabric Composites: Effect of Impact Parameters, *Journal of Reinforced Plastics and Composites*, 21: 1347–1362, 2002. <http://dx.doi.org/10.1177/0731684402021015294>
- [24] Y.Duan, M. Keefe, T.A. Bogetti, and B.A. Cheeseman, Modeling the role of friction during ballistic impact of a high-strength plain-weave fabric, *Composite Structures*, 68: 331–337, 2005. <http://dx.doi.org/10.1016/j.compstruct.2004.03.026>
- [25] Y.Duan, M.Keefe, T.A.Bogetti, and B.Powers, Finite element modeling of transverse impact on a ballistic fabric, *International Journal of Mechanical Sciences*, 48: 33–43, 2006. <http://dx.doi.org/10.1016/j.ijmecsci.2005.09.007>
- [26] V.B.C. Tan, V.P.W. Shim, and T.E. Tay, Experimental and numerical study of the response of flexible laminates to impact loading, *International Journal of Impact Engineering*, 40: 6245–6266, 2003.
- [27] M.P. Rao, G. Nilakantan and M. Keefe, B.M. Powers, and T.A. Bogetti, Global/Local Modeling of Ballistic Impact onto Woven Fabrics, *Journal of Composite Materials*, 43: 445–467, 2009. <http://dx.doi.org/10.1177/0021998308097684>